Aerosol source plume physical characteristics from space-based multiangle imaging

Ralph A. Kahn,[1] W.-H. Li,[1,2] Catherine Moroney,[1] David J. Diner,[1] John V. Martonchik,[1] and Evan Fishbein[1]

[1]   Models that assess aerosol effects on regional air quality and global climate parameterize aerosol sources in terms of amount, type, and injection height. The multiangle imaging spectroradiometer (MISR) aboard NASA's Terra satellite retrieves total column aerosol optical thickness (AOT), and aerosol type over cloud-free land and water. A stereo-matching algorithm automatically retrieves reflecting-layer altitude wherever clouds or aerosol plumes have discernable spatial contrast, with about 500-m accuracy, at 1.1-km horizontal resolution. Near-source biomass burning smoke, volcanic effluent, and desert dust plumes are observed routinely, providing information about aerosol amount, particle type, and injection height useful for modeling applications. Compared to background aerosols, the plumes sampled have higher AOT, contain particles having expected differences in Angstrom exponent, size, single-scattering albedo, and for volcanic plume and dust cloud cases, particle shape. As basic thermodynamics predicts, thin aerosol plumes lifted only by regional winds or less intense heat sources are confined to the boundary layer. However, when sources have sufficient buoyancy, the representative plumes studied tend to concentrate within discrete, high-elevation layers of local stability; the aerosol is not uniformly distributed up to a peak altitude, as is sometimes assumed in modeling. MISR-derived plume heights, along with meteorological profile data from other sources, make it possible to relate radiant energy flux observed by the moderate resolution imaging spectroradiometer (MODIS), also aboard the Terra spacecraft, to convective heat flux that plays a major role in buoyant plume dynamics. A MISR climatology of plume behavior based on these results is being developed.

Citation: Kahn, R. A., W.-H. Li, C. Moroney, D. J. Diner, J. V. Martonchik, and E. Fishbein (2007), Aerosol source plume physical characteristics from space-based multiangle imaging, *J. Geophys. Res.*, *112*, D11205, doi:10.1029/2006JD007647.

1.   Introduction

[2]   Most transport models used to assess aerosol effects on regional air quality and global climate are initialized with a set of aerosol source descriptions or emission inventories. These sources are usually parameterized with three quantities: source strength, aerosol type, and injection height [e.g., *Penner et al.*, 1994; *Ginoux et al.*, 2001]. Large-scale chemical transport models (CTMs) are the leading tools for predicting future aerosol impacts on climate [*Intergovernmental Panel on Climate Change (IPCC)*, 2001], and they provide some of the best ways to integrate disparate satellite, in situ, and surface aerosol observations into a global picture [e.g., *Ackerman et al.*, 2004; *Rasch et al.*, 2001]. Other models use similar source parameterizations at finer spatial scales to track the evolution of individual plumes for regional pollution exposure studies and air quality prediction [e.g., *Cotton et al.*, 2003; *Akimoto*, 2003].

[3]   Many aerosol types, such as desert dust, biomass burning, and anthropogenic particles, originate from discrete sources over land. The multiangle imaging spectroradiometer (MISR), flying aboard the NASA Earth Observing System's Terra satellite, routinely produces total column aerosol optical thickness (AOT) globally, about once per week, at 17.6 km horizontal resolution, over water and land [*Martonchik et al.*, 2002; *Kahn et al.*, 2005; *Abdou et al.*, 2005], including over bright desert surfaces [*Martonchik et al.*, 2004]. The Research Aerosol Algorithm can perform aerosol retrievals for selected patches at spatial resolutions down to better than 3 km. Covering a range of air mass factors from one to three, and a range of scattering angles from about 60° to 160° in midlatitudes, the instrument's nine cameras also provide some information about aerosol size, single-scattering albedo (SSA), and shape, which helps constrain aerosol type [*Kahn et al.*, 2001; *Kalashnikova and Kahn*, 2006; Chen et al., Sensitivity of multiangle imaging to optical and microphysical properties of biomass burning particles, submitted to *Journal of Geophysical Research*, 2007, hereinafter referred to as Chen et al., submitted manuscript, 2006].

[4]   The elevation of a reflecting layer above Earth's surface, as seen from space, is also routinely derived from

---

[1]Jet Propulsion Laboratory, California Institute of Technology, Pasadena, California, USA.

[2]Now at Northrop Grumman Space Technology, Redondo Beach, California, USA.

MISR data, by stereo-matching 275 m pixel resolution red-band multiangle observations [*Muller et al.*, 2002]. This global capability relies fundamentally on geometry, and unlike most other passive methods, does not depend on absolute radiometric calibration. The MISR operational level 2 Stereo Height product (TC_STEREO files from http://eosweb.larc.nasa.gov) reports heights above the geoid, to ±0.56 km, on a 1.1-km grid, of atmospheric features that are sufficiently well defined that they can be identified in multiple angular views [*Moroney et al.*, 2002].

[5] Since aerosols lofted into the free troposphere are often carried hundreds or thousands of kilometers downwind, whereas those confined to the boundary layer typically fill this well-mixed, near-surface layer but remain nearer the source region, plume height measurements, to a kilometer or better, are of major value for aerosol transport modeling. This is illustrated in the detailed 2002 Quebec fire investigation of *Colarco et al.* [2004]. They used an aerosol transport model, along with satellite imagery, to map the southward progress of smoke from the Quebec fires between 5 and 9 July. According to the model, the smoke gradually descended, until it reached the top of the planetary boundary layer near 2-km elevation on 7 and 8 July. Then the smoke mixed rapidly down to the surface, which, as observed, dramatically affected air quality in the Washington DC area. Aerosol injection heights in the source region were unconstrained by available data, and those inferred from back trajectories range from 2 to 6 km over the fire region on 5 July. This wide range of heights in the source region left room to account for most of the structure observed subsequently near DC, but did not constrain it well. A higher-altitude smoke concentration over DC predicted by the model for 7 July, though never directly observed, was assigned to smoke injected above 3-km elevation on 6 July. As discussed in their study, source-region moist convection that could have lifted smoke above the boundary layer was weaker on 6 July than on 5 July, raising questions about the validity of the higher-level feature produced by the model that could not be resolved.

[6] In the current paper, we compare MISR-retrieved background values with MISR aerosol source plume amount and type; these are related to the first two quantities usually used for model source characterization. We also explore in detail MISR constraints on source plume elevation, a measure of the third quantity, and examine the dynamical implications. The paper begins with a brief review of the MISR Stereo Height derivation, with emphasis on its application to aerosol source regions; this supplements the aerosol amount and type product descriptions published in the references cited above. We then analyze MISR-retrieved aerosol source-plume physical characteristics for representative wildfire, volcanic plume, and dust storm events. In the final section, we review the physical constraints derived, summarize their implications for plume dynamics, and draw conclusions aimed at continuing aerosol plume regional and global-scale studies.

2. MISR Aerosol Plume Stereo-Height Derivation Process

[7] The MISR Stereo Height retrieval algorithm is a two-stage process [*Moroney et al.*, 2002; *Diner et al.*, 1999]. An estimate of mean wind is derived at the reflecting level, on a coarse-resolution (70.4 km) grid fixed with the MISR product block structure. The grid-cell-average mean wind is obtained by comparing each of two triplets of images, the 70° and 45° forward + nadir views, and the 70° and 45° aft + nadir images, to an accuracy of about 1 to 3 m/s (6 m/s for pre-Version 14 stereo products) and 400 m vertical resolution. If the difference between these triplets is too large, the WindQA flag is set to "bad," the wind retrieval is rejected, and no wind-corrected heights are calculated.

[8] Then to derive the reflecting layer elevation, matching is performed between the 26°-forward and nadir views, and independently between the 26°-aft and nadir views, keying on the level of maximum reflectance contrast, and using the MISR 275 m spatial resolution red-band images over each 1.1-km horizontal region. Reflecting layer elevations are calculated from each fore and aft pair over an entire 70.4-km domain, and the mean and standard deviation of all fore-aft pairs is obtained. Then, for a 1.1-km pixel, if both pairs yield successful retrievals, and the fore-aft pair difference for that pixel is within two standard deviations of the domain mean elevation, the higher value obtained for that pixel is reported. This final step amounts to a constraint on elevation uniformity over the domain. If only one fore-aft pair yields a successful retrieval, the parallax from that pair is used.

[9] In the operational algorithm, stereo height matching is done with the near-nadir and nadir views to minimize the computational load required to identify corresponding features in multiple views; however, multilevel clouds and low-contrast scenes sometimes present difficulties. By specially processing steeper angle views with the MISR Research Stereo Height algorithm, optically thin plume detection, ~275 m vertical precision, and in some cases, discrimination of multiple layers, can be obtained. When the automated wind retrieval step is successful, standard product results are reported both for wind-corrected ("best winds") and uncorrected ("without winds") matches at 1.1 km. Typically, the without winds product provides more complete regional coverage, whereas best winds offers greater accuracy, especially when the plume is aligned with the multiangle viewing axis, which, away from the poles, is roughly north-south. One way to bridge the best winds and without winds products is to determine the regression relationship between the results for a given region, using those pixels having both, and to use that relationship to adjust the heights for pixels having only without winds values. This should be done individually over localized areas that are expected to have the same wind field, as demonstrated in section 3.1.2 below.

[10] MISR Stereo Height product sensitivity and accuracy have been validated against radar and lidar ground truth for cloud cases [*Moroney et al.*, 2002; *Naud et al.*, 2002, 2004, 2005], and similar results are expected for aerosol plumes, given the geometric nature of the method. The product has so far been heavily used for condensate cloud detection and analysis [e.g., *Seiz et al.*, 2007; *Seiz and Davies*, 2006; *Diner et al.*, 2005]. In aerosol source regions, especially biomass burning events, volcanic eruptions, and desert dust storms, aerosol plumes often make good stereo-matching targets, so the elevations of aerosol reflecting layers can be derived. The standard MISR Stereo Height product itself
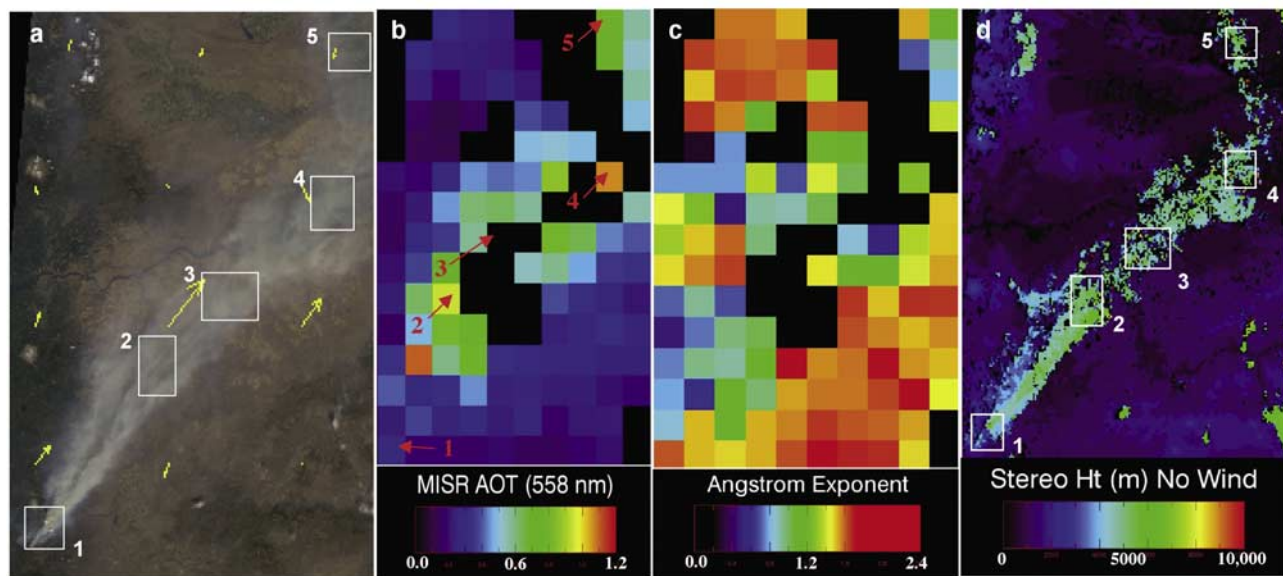
Figure 1. Oregon Fire, 4 September 2003, orbit 19753, path 044, blocks 53–55, ~19:00 UTC. (a) MISR nadir view of the fire plume, with five study site (patch) locations indicated as numbered white boxes (see Table 1), and MISR Stereo-derived wind vectors superposed in yellow. (b) MISR midvisible column AOT (version 17) retrieved at 17.6-km spatial resolution, with study site locations indicated by red arrows. There are no retrieval results for the black pixels, in most cases due to the high AOT and AOT variability of the plume core. (c) MISR-derived, column-average Angstrom exponent for the plume and surrounding area. (d) MISR Stereo Height product (version 13), without wind correction (labeled "no wind" in the figure), for the same region.

does not identify features as condensate or aerosol, since no algorithm is currently implemented to do this reliably for the range of common situations globally. Aerosol plumes must be identified as distinct from cloud or surface topography on a case-by-case basis, using independent criteria. Systematic identification of aerosol source plumes in the multiyear MISR record is under study, using support vector machine (SVM) pattern recognition methods [*Mazzoni et al.*, 2007]. With this technique, a database identifying aerosol source plumes in the multiyear MISR record is being developed as a resource for comprehensive aerosol emission inventory and source plume studies.

3. Aerosol Source Plume Physical Properties

[11] In this section, we use MISR and other data to characterize aerosol plumes produced by wildfires, volcanoes, and dust storms, highlighting one example in each category. The cases selected illustrate the key physical mechanisms expected in both free- and forced-convective aerosol plume formation, and represent far more than the dozen or so events we analyzed in detail for this study. A global sampling, allowing a statistical assessment of plume type differences, is part of continuing work.

3.1. Central Oregon "B&B Complex" Fire, 4 September 2003

[12] Figure 1a presents an ~130-km wide, natural color nadir view of the smoke plume emanating from the B&B Complex wildfire in central Oregon on 4 September 2003, ~19:00 UTC (Table 1). Five patches are marked in this image, for which detailed analysis follows. Patches here,

and for subsequent examples, were selected to sample the extent of the smoke plume to the degree possible, in areas having relatively high and uniform AOT. In most cases, patches cover a few hundred 1.1 pixels to assure adequate sampling because small numbers of pixels are more likely to be dominated by partly plume-filled pixels, skewed by complex, subpixel plume topography, etc. For the smaller patches, care was taken to determine, as much as possible, that these factors are not significant.

[13] The plume's NE orientation matches 24-hour modeled forward trajectories [*Draxler and Rolph*, 2003] for elevations between 3.5 and 6.5 km; below 3 km, the wind blows progressively more to the east. According to the model, the wind speed increases with height between 2.5 and 6.5 km elevation in the plume region. Also shown in Figure 1a are the MISR cloud-motion-derived wind vectors, assessed on 70.4-km retrieval domains from the steeply viewing cameras, and superposed as yellow arrows. The maximum wind speed (longest arrow) derived here is about 14 m/s, which compares well with 10–15 m/s from the forward trajectories. The burn area progression for this fire, spanning 20 August through 6 September, was mapped by the US Department of Agriculture Forest Service (http://www.fs.fed.us/r6/centraloregon/fires/2003/b-b/progression-map.shtml).

3.1.1. Particle Optical Properties

[14] Figure 1b shows the corresponding MISR standard green-band (558 nm) AOT product (version 17), which is reported over 17.6-km regions. AOT is a measure of aerosol amount, an instantaneous constraint on the time-integrated source strength; fire models usually obtain this quantity

Table 1. Fire, Volcano, and Dust Plumes Used in This Study

Event	Date	Time[a] (UTC) Terra Orbit	MISRPath /Block	Figures	Patch	Lat. (Upper Left)	Lon. (Upper Left)	Lat. (Lower Right)	Lon. (Lower Right)
Oregon Fire	4 September 2003	19:00 19753	044/53−55	1, 2, 3, and 4	P1	44.7	−121.8	44.5	−121.6
Oregon Fire	4 September 2003	19:00 19753	044/53−55	1, 3, and 4	P2	45.3	−121.0	45.1	−120.7
Oregon Fire	4 September 2003	19:00 19753	044/53−55	1, 3, and 4	P3	45.6	−120.5	45.4	−120.2
Oregon Fire	4 September 2003	19:00 19753	044/53−55	1, 3, and 4	P4	46.0	−119.7	45.7	−119.5
Oregon Fire	4 September 2003	19:00 19753	044/53−55	1, 3, and 4	P5	46.6	−119.4	46.4	−119.2
Colorado Fire	9 June 2002	17:50 13170	032/59−61	6a	−	39.9	−105.0	39.7	−104.8
Siberian Taiga Fire	11 June 2003	03:50 18506	130/47−49	6d	−	54.2	110.4	53.8	110.9
Canberra Fire	19 January 2003	00:00 16421	089/118−120	6g	−	-35.7	149.1	−35.9	149.4
Los Angeles Fire	26 October 2003	18:35 20510	040/63−64	6j	−	33.1	−118.6	32.9	−118.3
Mt. Etna Volcano	27 October 2002	10:00 15204	189/60−63	8 and 9	P1	37.8	15.0	37.7	15.1
Mt. Etna Volcano	27 October 2002	10:00 15204	189/60−63	8 and 9	P2	37.6	14.9	37.5	15.1
Mt. Etna Volcano	27 October 2002	10:00 15204	189/60−63	8 and 9	P3	37.4	14.9	37.1	15.0
Mt. Etna Volcano	27 October 2002	10:00 15204	189/60−63	8 and 9	P4	36.9	15.0	36.7	15.1
Mt. Etna Volcano	27 October 2002	10:00 15204	189/60−63	8 and 9	P5	36.5	14.7	36.2	15.0
Mt. Etna Volcano	29 October 2002	09:45 15233	187/60−62	8 and 9	E3	36.7	15.4	36.6	15.5
S. California Dust	27 November 2003	18:40 20976	040/64	11 and 12	P1	32.9	−117.2	32.8	−116.9
S. California Dust	27 November 2003	18:40 20976	040/64	11 and 12	P2	33.0	−117.7	32.7	−117.5
S. California Dust	27 November 2003	18:40 20976	040/64	11 and 12	P3	33.0	−118.1	32.8	−117.8
S. California Dust	27 November 2003	18:40 20976	040/64	11 and 12	P4	32.2	−117.7	33.0	−117.5
S. California Dust	27 November 2003	18:40 20976	040/64	11 and 12	P5	32.3	−118.1	33.1	−117.8
Bodele Dust	3 June 2005	09:27 29038	183/75−78	13a	−	16.2	17.6	16.0	18.7
Atlantic Dust	4 March 2004	11:55 22399	207/72−75	13d	−	21.4	−19.2	21.0	−18.8
Quebec Fire	6 July 2002	15:45 13562	013/55−58	14	P1	52.8	−78.5	50.9	−74.2
Adarondak Fire	6 July 2002	15:50 13562	013/55−58	14	P3	44.4	−77.8	40.7	−74.4

[a]Time accurate to ∼5 min for the nadir view; it takes about 7 min for all nine MISR cameras to view a location on Earth's surface.

from an empirical relationship between fuel type, fuel density, and observed burn area. In the plume core, the black regions indicate that no MISR AOT was retrieved by the Standard algorithm, in places because the AOT is too high for surface features to be observed through the plume at the steeper angles, and in others due to a lack of angle-to-angle correlation caused by geometric parallax in a structurally complex scene. In the plume periphery, midvisible AOT ranges from about 0.7 to over 1.0, distinctly higher than background AOT values. Similarly, in Figure 1c, the retrieved Angstrom exponent (ANG) in the plume periphery is less than about 1.4, smaller than that of the background; if these are monomodal distributions, this suggests that the plume particles are in the medium-small range, and are somewhat larger than the background aerosol. Other retrieval results, summarized in Table 2, indicate that the plume and background particles are predominantly spherical, and that the plume particles are more monodisperse and somewhat more absorbing than those in the background. Note that the aerosol products, other than the midvisible AOT and plume

Table 2. Summary of Aerosol Physical Characteristics for Plumes and Surroundings[a]

Region	AOT_{558}	ANG	SSA_{558}	Aerosol Type[b]
Oregon Fire, 4 September 2003 (Orbit 19753)				
Plume Periphery	≥0.7	<1.4	≤0.95	Spherical, SSA ∼ 0.8 to 0.9, r_{eff} ∼ 0.12
Background	≤0.3	≥1.4	∼1.0	Spherical, SSA ∼ 1.0, different sizes
Mt. Etna, 27 October 2002 (Orbit 15204)				
Plume Core	>0.5	<0.2	0.96±0.02	≥85% medium nonspherical (dust) + spherical, SSA ∼ 0.9 to 1.0, r_{eff} ∼ 0.12
Background	<0.2	>0.7	≥0.98	Spherical, SSA ∼ 1.0, r_{eff} ∼ 0.12 + 10−30% medium nonspherical (dust) (∼50% in isolated patches)
California Dust, 27 November 2003 (Orbit 20976)				
Plume Core	0.2−0.33	<0.3	0.93−0.96	≥40% medium nonspherical (dust) + spherical, SSA ∼ 0.9 to 1.0, r_{eff} ∼ 0.12
Background	<0.15	>0.8	0.95−1.0	Spherical, SSA ∼ 1.0, r_{eff} ∼ 0.06 + spherical, SSA ∼ 0.8, r_{eff} ∼ 0.12 or dust
R1[c]	0.55	∼0.0	0.90	40% medium nonspherical (dust) + 30% spheroids (coarse dust analog) + 30% spherical, SSA ∼ 0.8, r_{eff} ∼ 2.80
R2[c]	0.40	∼0.0	0.93	45% medium nonspherical (dust) + 55% spheroids (coarse dust analog)

[a]All results in this table, except R1 and R2, are from the MISR Standard Aerosol product, version 17. All AOT and SSA values in this table are reported at 558 nm (MISR Band 2). Reported quantities represent the range of retrieved values; uncertainties are discussed in section 3.1.1, and the cited references.

[b]Aerosol type percents are assessed based on contributions to the midvisible total column AOT, externally mixed. Percent component amounts are accurate to about 20% of the total AOT [e.g., *Kahn et al.*, 2001; *Kalashnikova and Kahn*, 2006; *Chen et al.*, 2006]. Dust is a nonspherical, medium, SSA ≥ 0.95 particle, which could be mineral dust or volcanic ash.

[c]Research retrieval results, for 3.3 × 3.3 km patches identified in Figure 11a. Near-ocean-surface wind speed is assumed to be 2.5 m/s; results are nearly identical if 0 or 5 m/s is assumed.
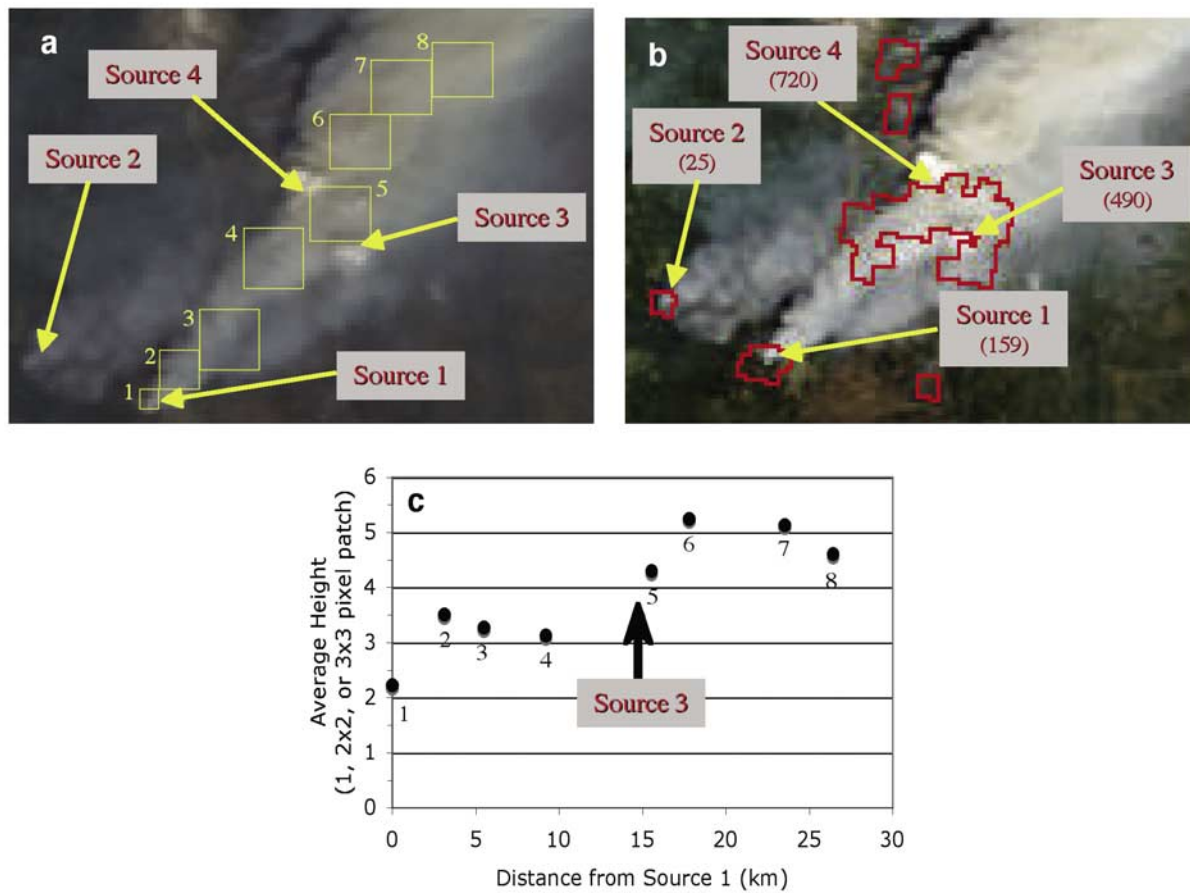
Figure 2. A detailed look at the plume source region within patch 1 of Figure 1a. (a) Image detail of the patch 1 region, from the MISR nadir view at 275-m horizontal resolution, showing fire fronts and pyrocumulus. Four of the major plume sources are labeled, and the yellow boxes indicate subpatches analyzed in Figure 2c. (b) MODIS Rapid Response image (http://rapidfire.sci.gsfc.nasa.gov/gallery) of the same area, with the regions where fires were detected based on the radiative energy flux outlined in red. Peak reported radiant energy fluxes (W/m^2) are given in parentheses with each source label. (c) MISR-derived plume height as a function of distance from source 1. Groups of one, four, and nine 1.1-km pixels were aggregated for this plot. The vertical resolution is about 0.5 km, and the approximate location of source 3 along the radius from source 1 is labeled.

height, are not yet validated globally. But distinct aerosol plumes, such as those included in this study, are sufficiently optically thick that the version 17 MISR-retrieved particle properties are reliable at the level of three-to-five size bins (small, medium, and large), two-to-four groupings in SSA (nonabsorbing vs. absorbing), and spherical versus nonspherical, making possible the separation of about a dozen aerosol air mass types based on particle properties, and allowing us to distinguish plume and background aerosols [*Kahn et al.*, 2001, 2005; *Kalashnikova and Kahn*, 2006; Chen et al., submitted manuscript, 2006].

3.1.2. Plume Height

[15] Figure 1d shows the corresponding MISR Stereo Height standard product (without winds, version 13). Here much of the plume top appears to reside at about 5 km above the geoid and is colored green in the image. For patch 1, the land surface is up to 1.3 km above the geoid, but very variable. For patches 2 and 3, surface elevation is about 0.5 to 0.7 km, and for patches 4 and 5, 0.1 to 0.3 km. Away

from the surface, elevation above the geoid is often better matched than height above the local terrain to constant atmospheric pressure surfaces along which air masses, including smoke plumes, are likely to travel.

[16] Several fire fronts near the upwind edge contribute to plume branches that appear to split within patch 1 in Figure 1a, and are shown as green and blue plumes in Figure 1d. The patch 1 sources appear in more detail in Figures 2a and 2b, which are MISR and moderate-resolution imaging spectroradiometer (MODIS, also flying aboard the Terra satellite) images, respectively. The fire fronts observed by MISR also stand out in the MODIS fire product, for which areas emitting large amounts of thermal infrared radiation are outlined in red.

[17] The upwind fire front at MISR overpass time (designated source 1) appears toward the lower left of patch 1. Additional major fire sources are found in the extreme lower left (source 2), and 15 to 17 km downwind of source 1, near the center of this patch (sources 3 and 4 and possibly
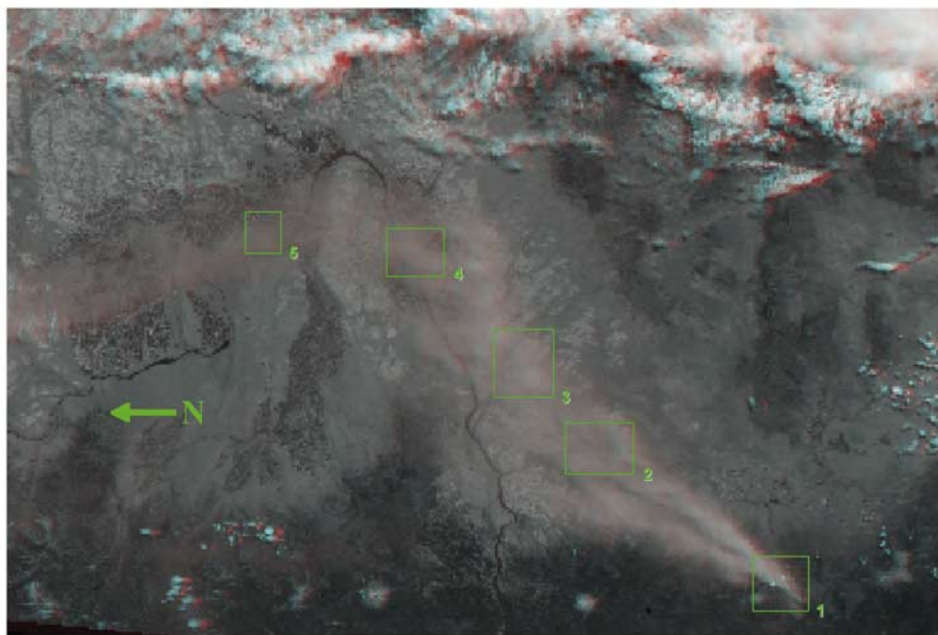
Figure 3. Red-blue stereo anaglyph of the Oregon Fire plume, 4 September 2003, constructed from the MISR 26° forward and aft red-channel images. As indicated on the image, north is to the left, unlike other images in this paper, to make stereo viewing possible. The rise and asymptotic elevation of major plumes can be seen in spatial context, along with the pyrocumulus associated with sources in patch 1, a high cloud system to the east (top), and a few isolated cumulus to the west (bottom). There is also a hint of the surface topography, especially that of the river valley at center in the lower part of the image. For proper viewing, use red-blue glasses, with the red lens over the left eye; cardboard glasses with plastic lenses are available inexpensively over the Web, and at some stationary and toy stores. Some people find incandescent or natural lighting works better than fluorescent for viewing.

points between), where dense smoke and bright white dots occur, likely pyrocumulus clouds driven by intense heat sources. Comparing with the lower-resolution Figure 1, the plume branch associated with source 2 appears light blue, and is about a kilometer lower than that associated with sources 3 and 4.

[18] Examination of the stereo anaglyph in Figure 3, made from the MISR 26° forward and aft red images, provides a more graphic view of the multiple smoke sources in this scene (see Figure 3 caption for anaglyph viewing instructions; for this image, north is to the left). From the spatial relationships evident in Figures 2a, 2b, and 3, source 1 originates to the south and east of source 2, rises more rapidly, and initially reaches a greater altitude. Continuing downwind, the plumes from sources 1, 3, and 4 seem to merge.

[19] Figure 2c reports quantitative plume elevations from the 1.1-km horizontal resolution product, for eight sub-patches marked in yellow in Figure 2a, at progressively greater distances from source 1. There is scatter in these data since each point represents an average of only 1, 4, or 9 pixels, and the inherent vertical resolution of each value is about 0.5 km. The plot shows a progression from near surface to about 3 km within about 5 km of source 1, and a second phase of lofting 15 to 17 km downwind, near sources 3 and 4, supporting the idea of a second, probably more intense fire front, that generates smoke, pyrocumulus, and additional buoyancy.

[20] MISR observed over 400 km of the aggregated plume extent, providing an indication of its evolution.

Figures 4a–4e give an overview of retrieved elevations for the five patches spanning the entire plume marked in Figure 1. For patch 1, which includes the major sources, the spread of retrieved heights reflects buoyant lofting of initially hot plumes as they progress downwind. The smoke appears to stabilize further downwind at about 5.5 ± 0.5 km above the geoid. By patches 3, 4, and especially 5, gradual thinning has occurred, with no evident change in upper-level plume elevation. An additional, near-surface aerosol layer appears in patches 4 and 5. This lower layer is aerosol within the boundary layer, probably from less buoyant sources downwind of the primary source region. The heights of multiple layers appear in these histograms because, within a patch a few hundred pixels on a side, the smoke optical thickness varies, and the level of maximum contrast usually captures more than one layer, if several exist. The layering, identified in the MISR data, is key to aerosol transport calculations, as discussed in section 4.

3.1.3. Elevation Adjustments for Regional Wind

[21] The retrieved without winds plume height values can be adjusted to account for regional wind by deriving a height regression relationship between the without winds and best winds retrievals for those pixels having both, and then applying it to pixels having only without winds retrievals. The implied adjustments are small. For an along-track wind component of 10 m/s, the height adjustment for a single pixel, assessed for a 26° MISR camera, is about 0.35 km. For patch 1, applying the regression line raises the without winds heights by an offset
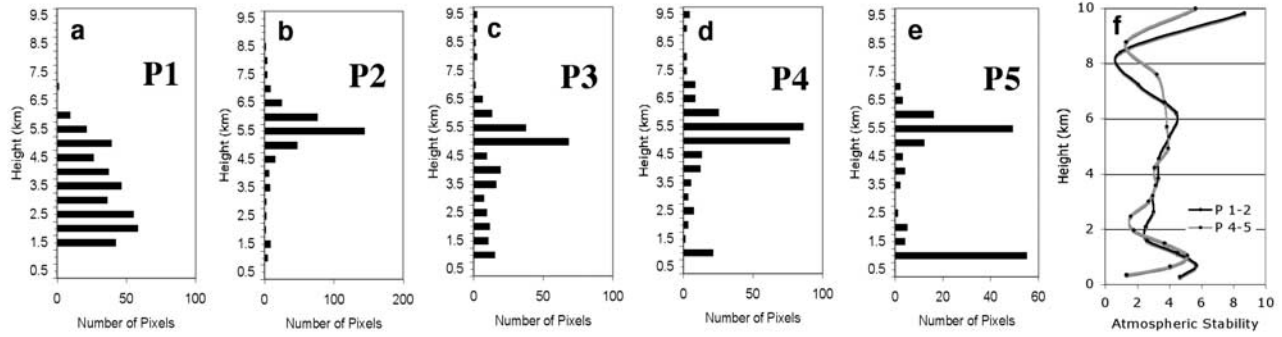
Figure 4. (a−e) Histograms of MISR Stereo standard product plume height for the five study sites identified in Figure 1a, retrieved at 1.1 km horizontal resolution, and about 0.5 km vertical resolution. (f) Atmospheric stability profiles derived from the NCEP GDAS [*Saha et al.*, 2005], at about 50 km horizontal resolution, assessed in the vicinity of patches 1 and 2 (black) and patches 4 and 5 (gray). The average local elevation above the geoid in the study region varies from over +1 km over much of patch 1, to below +0.2 km in patch 5; elevations in the figures are all referenced to the geoid, taken to be a standard pressure surface (see text).

of about 0.44 km, and reduces the effective regression line slope by about 1%. For patch 2, the corresponding numbers are 0.92 km higher and 7% lower, and for patch 4, they are 0.28 km higher and 1% lower. These regression results each include about a half-dozen outliers that, if removed, further diminish the required height adjustments. The adjusted offset for patch 1 is 0.31 km, with an R^2 of 0.99, for patch 2, 0.56 km with $R^2 = 0.997$, and for patch 4, 0.17 km with $R^2 \sim 1.0$. For each regression, the number of cases (N) is between 300 and 400. The regression plot for patch 2 is given in Figure 5.

[22] In addition to natural scatter in the data, the mean wind component that runs along the spacecraft track (roughly NNE-SSW at these latitudes) contributes to the regression line offsets. Once outliers are removed, the regression line slopes are essentially unity. This is expected because the MISR Standard wind algorithm does not retrieve vertical wind shear. The mean wind correction affects regression line offsets but not slopes, since it adds only a constant factor to the parallaxes of cloud elements at all levels in a 70.4-km domain. The wind is assessed by the stereo matching algorithm at the level of maximum reflectance contrast; for patches 1, 2, and 4, the parallaxes at these levels correspond to elevations of >4.2, >4.4, and <10.0 km, respectively. Though it is beyond the capability of the current operational algorithm, where MISR sampling and scene variability make it feasible to assess the wind vectors on spatial domains smaller than 70.4 km, vertical wind shear can be derived from MISR data along with wind vectors, on horizontal spatial scales appropriate for aerosol source plumes.

3.1.4. The Relationship Between Plume Height and Atmospheric Stability Structure

[23] Plotted in Figure 4f, on a vertical scale similar to that of the plume-height histograms, is ambient atmospheric stability relevant to patches 1 and 2 (black curve) and patches 3 and 4 (gray curve). This quantity is assessed as the vertical gradient of the potential temperature [e.g., *Holton*, 1992] derived from the NCEP Global Data Assimilation System (GDAS)

[*Saha et al.*, 2005], a model result reported every three hours at about 50 km horizontal resolution:

$$S = \frac{d\vartheta}{dz} \tag{1a}$$

with potential temperature:

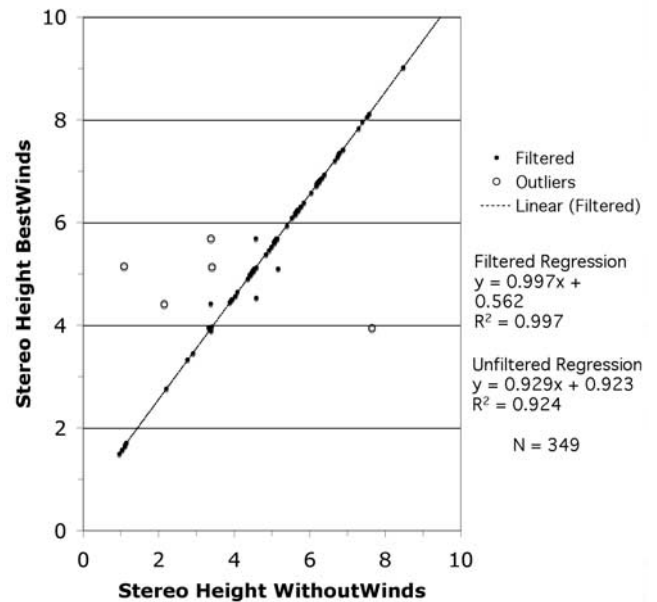$$\vartheta = T\left(\frac{p_0}{p}\right)^{R/c_p} \tag{1b}$$

Figure 5. Scatterplot between MISR Stereo Height best winds and without winds results, and linear correlation analysis, for patch 2 of Figure 1a. The outliers are identified as open circles, and the regression parameters are given on the right for both the full data set, and the data set filtered to remove the outliers.

T and p are the atmospheric temperature and pressure, respectively, at height (z), p_0 is the reference level pressure (taken as 1000 mb), R is the gas constant for dry air, and c_p is the specific heat for dry air at constant pressure. Negative values of S represent buoyant instability to small vertical displacements, zero corresponds to neutral stability, and larger values of S imply atmospheric regions where buoyancy is less likely to mix the air vertically. The ambient atmosphere in Figure 4f has typical structure; it is stable throughout, as might be expected, especially in the high-pressure conditions that favor wildfires. The nearest GDAS profile in space and time is displayed in this and other figures in the paper. Given the inherent resolution of the model, and uncertainties in initial and boundary conditions, there is little point to interpolating in space or time.

[24] To review the general properties of the stability profile in Figure 4f, near the surface is a time-dependent boundary layer, usually 1 or 2 kilometers thick at midday, that is generally stable at night; as the surface warms, a region of reduced stability forms near the ground and grows thicker as warming continues. Above the thermal boundary layer is a mixed layer, often identified as the lowest part of the free troposphere, whose temperature structure is dominated by convection. The stability of this layer varies little with height and is usually close to neutral or slightly positive. The mixed layer is surmounted by an inversion layer, whose higher thermal stability is mediated by warming due to subsidence in high-pressure systems. Diabatic heating of absorbing (smoke) particles at these levels can complicate the stability structure.

[25] The plume vertical distribution appears to be related to atmospheric stability, also as might be expected. The plume's initial buoyant ascent carries aerosol past the stable upper part of the boundary layer and through the mixed layer, to the relatively stable layer between about 5 and 6.5 km, where it concentrates. By relatively stable, we mean that the atmospheric stability is lower both above and below the layer containing the smoke. Aerosol also concentrates at about 1-km elevation, within the near-surface, high-relative-stability region of patches 4 and 5, possibly originating from local sources having less initial buoyancy than the main fire fronts.

[26] Figure 6 shows the relationships between vertical distribution and atmospheric stability for a collection of other, geographically distributed wildfire plumes: forest fires near Denver, Colorado, south-central Siberia, and near Los Angeles, and a brush fire near Canberra, Australia. Like the Oregon B&B Complex fire of Figures 1, 2, 3, and 4, all have vertical plume structure concentrated within relatively stable atmospheric layers, though the initial buoyancy, stability structure, and vertical wind shear vary from case to case.

[27] Specifically, for the Denver event (Figure 6a), in the source region, the plume histogram (not shown) exhibited two peaks, one at about 3.5 km, the other at about 7.0 km. The 7.0-km peak persists downwind, and appears in Figure 6b. For seven other patches scattered around the highlighted patch of the Siberia wildfire (Figure 6d), both the histograms and the atmospheric stability profiles (not shown) are similar to those given in Figures 6e and 6f, respectively, with plume height histogram peaks falling in the range of 2.5 and 3 km. A similar observation is made for eight patches covering the Canberra grassland fire

(Figure 6g), with all plume height histogram peaks in the range 2.5 to 3.5 km. And for the Los Angeles wildfire, six patches extending from near the source to beyond the patch highlighted in Figure 6j were examined. The near-source, over-land histograms (not shown) yield plume height peaks between 1.0 and 1.5 km; downwind, the smoke fills a layer between about 1.5 and 2.5 km, as illustrated in Figure 6k.

[28] So after initial injection, in these and other cases we have studied, the aerosol rises rapidly to an elevation that is affected by the convective heat flux at the source and the atmospheric stability profile. The aerosol concentrates within the boundary layer or layers of relatively high stability aloft. Aerosol that penetrates the near-surface boundary layer ascends further, and accumulates in a higher layer of relative stability; this occurs for larger forest fires, but aerosol plumes from smaller forest and grassland fires among the cases studied here remained confined to the boundary layer.

[29] Many aerosol transport models assume that aerosol plumes travel upward to an altitude determined only by the initial buoyancy, independent of the atmospheric stability structure [e.g., *Lavoué et al.*, 2000], and/or that the aerosol is uniformly distributed even when it reaches a height above the boundary layer. The observations presented here suggest that atmospheric stability must be taken into account as well. In the next subsection, we explore the constraints on plume dynamics that can be derived from these observations.

3.1.5. Constraints on Plume Dynamics

[30] Data from the MODIS instrument provides additional constraints on fire plume behavior. The MODIS fire product identifies fire source locations (Figure 2b) and estimates of fire area. Radiant energy flux is also reported based on an interpretation of data from two 4-μm channels and one 11-μm channel (MODIS bands 21, 22, and 31). Each product is given at 1 km horizontal resolution [*Justice et al.*, 2002; *Kaufman et al.*, 1998, 2003; *Giglio*, 2005]. The radiant energy flux (W/m^2) is obtained by matching the MODIS measured infrared radiance with a blackbody curve; it is used as an indicator of fire phase (flaming versus smoldering) and fire intensity. Note that the radiant energy observed at TOA by MODIS can be affected by fire phase, fire emissivity, and atmospheric obscuration by clouds and thick aerosol.

[31] MODIS data for the 4 September 2003 B&B Fire Complex at Terra overpass time locate the source region in parts of several 1 km pixels, including those at source 1, and more intense sources 3 and 4, as shown in Figure 2 (MODIS Product MOD-14, Collection 4, Granule MOD14.A2003247. 1900.004.2003257230023). Averaged over a 1-km^2 area, the pixel having the highest observed radiant energy flux (720 W/m^2) is associated with source 4, and is likely to contain the most intense fire in this scene.

[32] A fire model is needed to tie together MISR plume height observations, radiant energy flux derived from MODIS, and the atmospheric stability structure obtained from the NCEP GDAS. Previous attempts have been made to correlate plume height directly with radiant energy flux. But the relationship between the observed radiant energy flux and the convective heat flux that drives plume buoyancy depends on fuel type, fire phase, and environmental conditions, which must be part of a complete plume dynamics analysis. Several heuristic plume models, developed from basic thermodynamic principles, account for
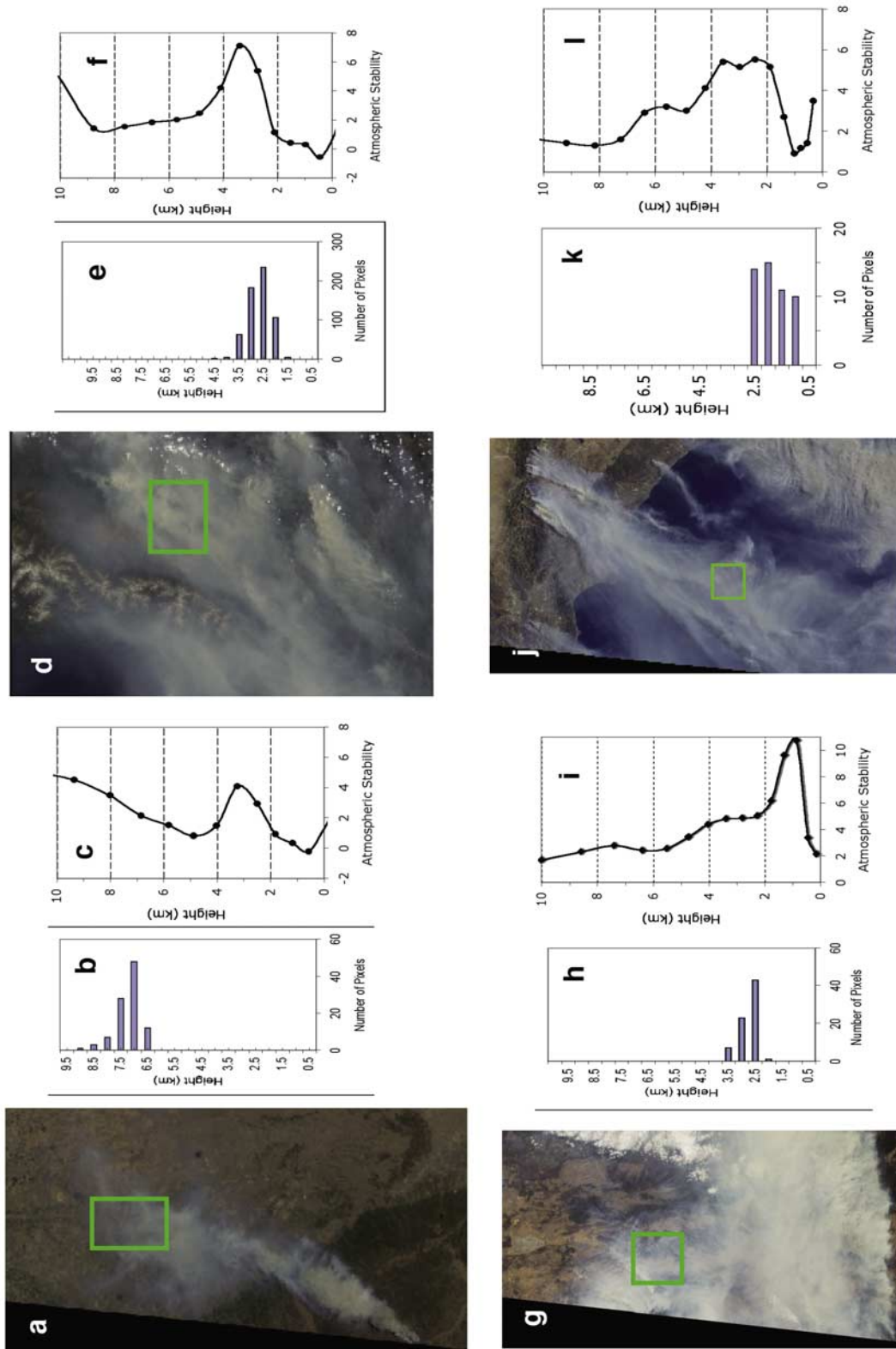
Figure 6. Fire plume height and atmospheric stability. (a–c) 9 June 2002 fire originating 65 km SW of Denver, CO (about 37–39°N lat, 105°W lon), orbit 13170, path 032, blocks 59–61. (a) MISR true-color nadir image with study patch marked in green. (b) Plume height histogram for the study patch, from MISR Standard Stereo Height product. (c) Atmospheric stability profile, calculated from the NCEP GDAS [*Saha et al.*, 2005] using equations (1a) and (1b). (d–f) Same as Figure 6a–6c, but for the 11 June 2003 fire in the Siberian Taiga, south of Lake Baikal (about 51–54°N lat, 110–112°E lon), orbit 18506, path 130, blocks 47–49. (g–i) Same as Figure 6a–6c, but for the 19 January 2003 brush fire near Canberra, Australia (about 35–37°S lat, 148–151°E lon), orbit 16421, path 089, blocks 118–120. (j–l) Same as Figure 6a–6c, but for the 26 October 2003 wildfires near Los Angeles (about 32–35°N lat, 117–120°W lon), orbit 20510, path 040, blocks 63–64.

aspects of plume dynamics [e.g., *Morton et al.*, 1956; *Weihs and Small*, 1993] and a range of more elaborate numerical models has been applied to early stage plume evolution processes for regionally significant wildfire and volcanic events [e.g., *Small and Heikes*, 1988; *Westphal and Toon*, 1991; *Clark et al.*, 1996; *Glaze et al.*, 1997; *Colarco et al.*, 2004; *Trentamnn et al.*, 2006, and references therein].

[33] As a simple first step to investigate the plausibility of the scenario advanced in section 3.1.4, we develop here a one-dimensional convective parcel model for a quiescent atmosphere, constrained by just the plume height and atmospheric stability profile. With this model, we explore parametrically the relationship between the dynamically important convective heat flux and the observed plume height.

[34] The buoyant acceleration of a parcel due to a temperature difference with its surroundings can be written [e.g., *Holton*, 1992]:

$$\frac{dw}{dt} = \frac{1}{2}\frac{d(w^2)}{dz} = g\frac{(T_p(z) - T_a(z))}{T_a(z)} + F_d \quad (2a)$$

where w is the parcel vertical velocity, g is the gravitational acceleration, T_a and T_p are the atmospheric and parcel temperatures, respectively, and F_d represents the dissipative force per unit mass, which includes cooler (and possibly drier) ambient air entrainment, and momentum mixing between the rising plume and its surroundings. For a crude representation of F_d, we assume that the flux of environmental mass into the plume uniformly carries momentum, heat, and moisture, which are all conserved in the mixing process. So the change in plume velocity (δw) is related to the mass from the surroundings that is added to the plume mass (δm) and the vertical velocity of the surroundings (w_s). Equating the locally final parcel momentum with the original plus the entrained:

$$(m + \delta m)(w + \delta w) = mw + w_s\delta m$$

Simplifying, ignoring the second-order term, and dividing by $m\delta t$:

$$\frac{\delta w}{\delta t} = (w_s - w)\frac{1}{m}\frac{\delta m}{\delta t} = (w_s - w)w\frac{\delta \ln(m)}{\delta z}$$

Setting $w_s = 0$ for a quiescent atmosphere, the entrainment drag becomes:

$$F_d(z) = -w^2\frac{d\ln(m)}{dz} = -\lambda w^2 \quad (2b)$$

We treat λ as a constant, free parameter, representing all the physics of entrainment in this simple model. We also assume the parcel follows a constant lapse rate (Γ_p):

$$T_p(z) = T_p(0) - \Gamma_p z \quad (3)$$

Substituting equations (2b) and (3) into equation (2a) yields an ordinary differential equation in w^2:

$$\frac{d(w^2)}{dz} + 2\lambda w^2 = 2g\frac{(T_p(0) - \Gamma_p z - T_a(z))}{T_a(z)} \quad (4a)$$

It has the solution:

$$w^2(z) = ae^{-2\lambda z}$$
$$+ 2g\int_0^z \frac{\left([T_p(0) - \Gamma_p \cdot z'] - T_a(z')\right)}{T_a(z')}e^{-2\lambda(z-z')}dz' \quad (4b)$$

where a is a constant. We evaluate equation (4b) for fixed values of λ, subject to $w = 0$ at $z = 0$ (so $a = 0$), and choose the dry adiabat as the representative parcel lapse rate (Γ_p), 9.8 K/km (that is, we assume that only dry processes affect the parcel). For the nominal atmospheric temperature profile, $T_a(z)$, we take the NCEP values, but we also consider atmospheric profiles having constant lapse rates of 5 and 6 K/km, representing moist pseudoadiabats. Subsequent plume evolution, not modeled here, could involve sinking to compensate for the negative buoyancy created as the rising plume overshoots its equilibrium level to reach the $w = 0$ elevation. In this case, overshoot appears to be less than the 0.5-km vertical resolution of the observations, since the plume levels off downwind within the local atmospheric stability maximum, and at the 1-km horizontal resolution of the observations, this corresponds to the peak altitude recorded in the source region. We evaluate equation (4b) at $z = H_p$, where H_p is the observed height to which the plume rises (between about 5.5 and 6.5 km from Figure 4), integrating numerically the terms on the right side involving $T_a(z)$ between 0 and H_p, and for each value of λ, solve iteratively for the value of $T_p(0)$ that yields $w(H_p) = 0$.

[35] The results for the B&B fire complex are plotted in Figure 7 over a range of λ, for the three atmospheric profiles, and with $H_p = 6.6$ km; Table 3 gives numerical values for the $\lambda = 0$ and $\lambda = 1$ cases, and for $H_p = 6.6$, 5.6, and 3.6 km. The $\lambda = 0$ case, which can be evaluated directly from equation (2a), represents an extreme lower bound on $T_p(0)$ required for the vertical velocity to go to zero at H_p in each case. For example, with $\lambda = 0$, $H_p = 6.6$, and the NCEP atmospheric temperature profile, $T_p(0) \sim 305$ K, producing a lower bound of about 490 W/m^2 for the fire's convective heat flux, 45 W/m^2 above the background surface temperature, based on the NCEP profile. More realistic cases have nonzero λ the value of which depends on the poorly known mass fraction that is entrained. Figure 7 shows that as λ increases and entrainment dominates, the $T_p(0)$ required for the plume to reach the observed elevation finds an asymptote; the plume vertical velocity becomes very slow, the plume accumulates minimal inertia, and parcel acceleration is determined locally. For each atmosphere, the asymptotic convective heat flux at the surface, above the background value, is about double that for the $\lambda = 0$ case. Given the short horizontal distance over which the plume reaches its peak altitude, to the extent that this model represents plume dynamics, values of λ less than or about 1 seem more likely to match the observations.

[36] The dynamical heat fluxes from this very simple model fall below the highest radiant energy flux observed by MODIS in the region (source 4, 720 W/m^2), but according to Table 3, would be higher than the peak fluxes recorded at the other source locations (159, 25, and 490 W/m^2 for sources 1, 2, and 3, respectively). Limitations of the model, in our knowledge of the local temperature and humidity profiles (for example, the $\sim$50 km resolution and other uncertainties of the
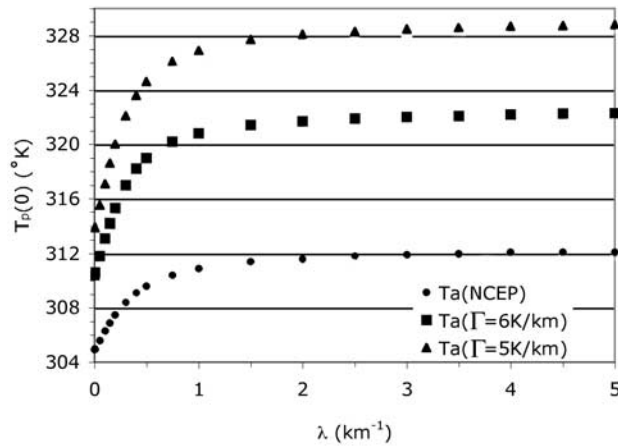
Figure 7. Fire convective energy flux required for an aerosol plume to reach 6.5 km elevation, expressed as plume parcel temperature at the surface ($T_p(0)$), plotted as a function of entrainment parameter (λ), according to the simple model of equations (4a) and (4b). Results are shown for three atmospheric temperature profiles: the NCEP GDAS profile corresponding to the B&B Complex fire source area, and constant lapse rates (Γ_a) of 5 and 6 K/km. The NCEP ambient temperature profile used in this calculation has about 50-km horizontal resolution, which covers the highlighted sources. Additional cases are given in Table 3.

NCEP results), and in MISR and MODIS spatial sampling scales, can easily account for these discrepancies. Unmodeled moist convection could alter the dynamical heat flux needed to reach H_p, and more complex entrainment could either increase or reduce the required energy. The MODIS-derived radiative energy flux is affected by the spectral fire emissivity assumed in the retrieval algorithm, the fire phase, and the possibility of cloud or thick smoke in the column reducing the observed TOA reflectances. These factors would reduce the measured radiative energy flux relative to the required dynamical heat flux. Also, the radiant heat sources may be smaller than the satellite pixel resolution, or the plume may be driven by heating aggregated over several MODIS pixels, making the MODIS-retrieved energy released per unit area lower or higher than the dynamical heat flux, respectively. So the exercise performed here demonstrates plausibility; both more advanced modeling and better knowledge of ambient conditions during the fire would tighten these constraints.

3.2. Mount Etna Eruption, 27 October 2002

[37] During 2002, the aerosol plume emanating from Mount Etna, Sicily, was captured a number of times by MISR. The October 27 observations, at about 10:00 UTC, are presented in Figure 8. The plume advects to the SSW, across the Mediterranean toward Algeria, consistent with forward trajectories at elevations between 2.5 and 6.5 km [*Draxler and Rolph*, 2003], as well as with the MISR stereo-derived wind vectors superposed in Figure 8a as yellow arrows. The peak wind (longest arrow) is about 12 m/s. Below about 2.5 km, the forward trajectory winds blow progressively more toward the west.

[38] The Etna plume core is optically thinner than that of the Oregon Fire, so the MISR Standard Aerosol algorithm retrieves AOT at most points in the plume over water (Figure 8b). Over the land surface of Sicily, the standard algorithm does not report aerosol retrieval values in the plume core, due to topographic complexity around the volcano itself, and downwind, primarily caused by AOT variability, which is assessed as a lack of angle-to-angle correlation by the algorithm's automatic cloud-masking process [*Martonchik et al.*, 2002].

[39] As with the Oregon fire plume, the aerosols generated by this event are distinct from those of the background, having higher AOT, lower ANG and lower SSA (Table 2 and Figures 8b and 8c). Figure 8d shows that within the plume, the aerosol mixtures in the standard retrieval algorithm providing the closest fit to the observed radiances are also distinct from those of the surroundings. In MISR Standard aerosol algorithm version 17, there are 74 mixtures; mixtures 1 through 30 contain mono- or bimodal spherical nonabsorbing particles, those from 31 to 50 are monomodal or bimodal and include spherical absorbing particles, and those above 50 have nonspherical dust analogs along with spherical particles. For most of the best-fitting mixtures within the plume, the algorithm assigns more than 50% of the midvisible AOT to medium, nonspherical, weakly absorbing particles characteristic of volcanic ash. The remainder is medium, spherical, and nonabsorbing or somewhat absorbing, which may be a mix of background aerosol, smoke, and other volcanic aerosols.

[40] Figures 9 and 10 provide more detail about plume development. Patch P1 encompasses the source region, and exhibits a range of stereo heights (Figure 9a). An analysis similar to that given for the B&B Complex Fire, and examination of a stereo anaglyph (not shown), indicate that the aerosol ascends to about 5.5 km above the geoid before it is advected more than a few kilometers downwind of the volcano. The histogram for P1 is complicated by two factors:

Table 3. Simple Plume Model Results[a]

H_p, km	Γ_a, K/Km	T_0, K ($\lambda = 0$)	F, W/m^2 ($\lambda = 0$)	T_0, K ($\lambda = 1$)	F, W/m^2 ($\lambda = 1$)
6.6	(NCEP profile)	305	490	311	530
6.6	6	310	526	321	601
6.6	5	314	550	329	648
5.6	(NCEP profile)	305	489	308	510
5.6	6	308	513	317	573
5.6	5	311	533	322	612
3.6	(NCEP profile)	302	470	304	484
3.6	6	305	487	309	518
3.6	5	306	498	312	539

[a]$\lambda = 0$ cases give a lower bound on surface temperature and corresponding dynamical heat flux required for the fire plume to reach H_p in equilibrium, and $\lambda = 1$, likely a more realistic value.
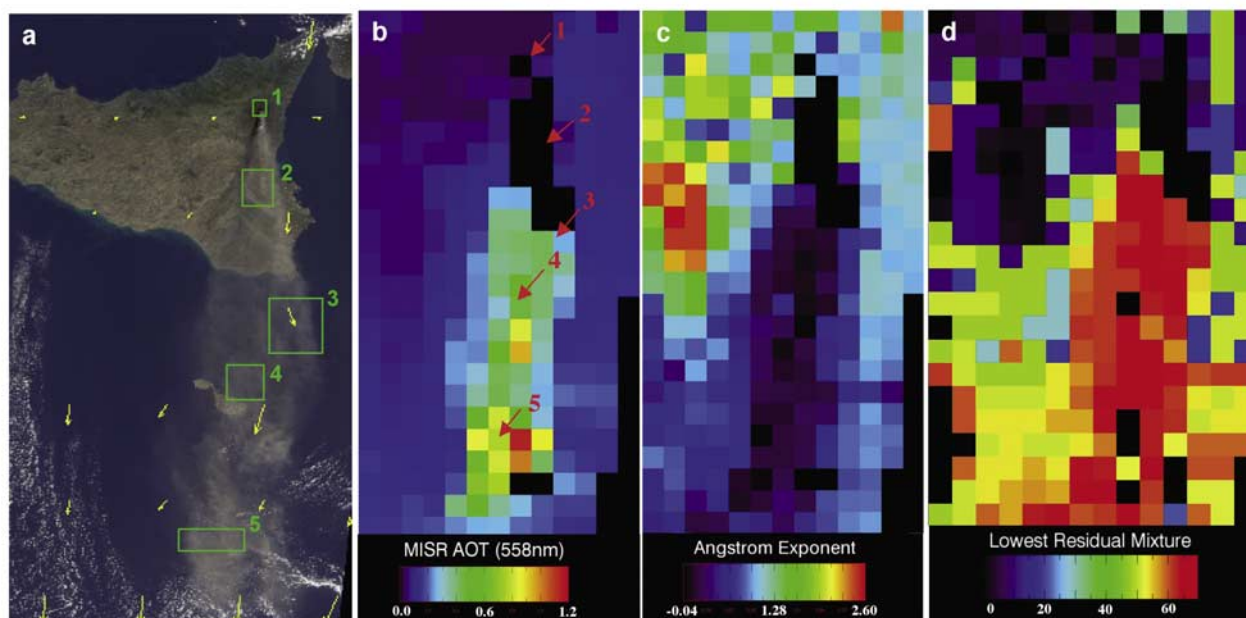
Figure 8. Mount Etna eruption, 27 October 2002, orbit 15204, path 189, blocks 60–63. (a) MISR nadir view of the volcano plume, with five study site (patch) locations indicated as numbered green boxes, and MISR Stereo-derived wind vectors superposed in yellow. (b) MISR midvisible column AOT (version 17) retrieved at 17.6 km spatial resolution, with study site locations indicated by red arrows. For the black pixels, no retrievals were obtained, in most cases due to high AOT or surface complexity. (c) MISR-derived, column-average Angstrom exponent for the plume and surrounding area. (d) MISR lowest-residual aerosol mixture for the same region. Mixtures 51–74 (shown in yellow and red) contain some nonspherical, weakly absorbing particles, whereas mixtures <51 contain only spherical particles, having a range of sizes and SSA, in varying proportions.

the topography of Mt. Etna itself, and multiple aerosol sources on the mountain. The volcano peaks at about 3.3 km. Reduced to 1.1-km horizontal resolution, the volcano top registers just over 3 km, and patch 1 includes topography roughly between 1.5 and 3 km elevation. So below 3.5 km, the histogram in Figure 9a is at least partly due to the surface. At 3.5 km and above, the histogram reflects plume. At higher

horizontal resolution (Figures 10a and 10b), several plume sources are resolved. Although it is not entirely clear in the Standard aerosol retrievals (for example, Table 2) or the MISR and MODIS images, these include multiple volcanic vents emitting steam ash, and gasses on both the NE and S slopes of the volcano, as well as one or more wildfire smoke plumes, probably triggered by hot lava or other volcanic
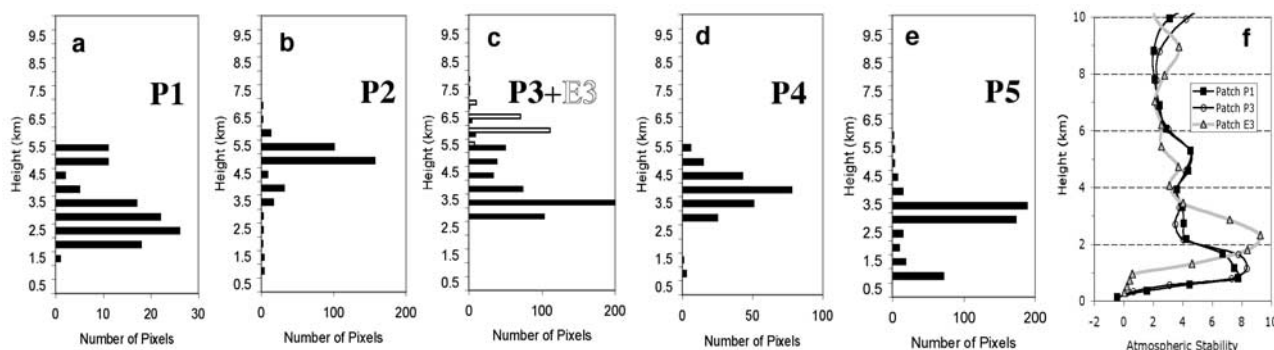

Figure 9. (a–e) Histograms of MISR Stereo standard product plume height, retrieved at 1.1 km horizontal resolution, and about 0.5 km vertical resolution, for the five study sites identified in Figure 8a. (f) Atmospheric stability profiles derived from the NCEP GDAS [*Saha et al.*, 2005], at about 50 km horizontal resolution, assessed in the vicinity of patch 1 (black line with squares) and patches P2 and P3 (gray line with circles). Also shown in Figure 9c are gray histograms for site E3, nearly colocated with P3, but obtained 2 days later, on 29 October 2002, orbit 15233, path 187. The corresponding atmospheric stability profile is given in Figure 9f as a gray line with triangles.

Figure 10. A detailed look at the plume source region within patch 1 of Figure 8a. (a) Image detail showing part of the patch 1 region, from the MISR nadir view at 275 m horizontal resolution, hints at the complex array of sources and pyrocumulus in the vicinity of Mt. Etna at overpass time on 27 October 2002. (b) MODIS Rapid Response image (http://rapidfire.sci.gsfc.nasa.gov/gallery) of roughly the same area as Figure 10a, with the regions where major heat sources were detected based on the infrared radiative energy flux outlined in red. (c) A high-resolution image looking toward the SW, acquired from the International Space Station on 30 October 2002, reveals the complex mix of steam, ash, and wildfire smoke plumes concentrated along both the NE (lower left-center in the image) and S (upper right) flanks of Mt. Etna. (Image ISS005-E-19015, obtained from the NASA Space Station on-line image gallery: http://spaceflight.nasa.gov/gallery/images/station/crew-5/html/iss005e19024.html). The major eruptions began about 12 hours before the Terra overpass. More details about ground-based observations of the 2002 Etna eruption are given by: http://boris.vulcanoetna.com/ETNA_2002.html and http://www.swisseduc.ch/stromboli/etna/etna02/etna0211northfissure-en.html.

effluent. These features are better observed in a yet higher-resolution image of the volcano taken from the International Space Station on 30 October (Figure 10c).

[41] The MISR and MODIS data also show several small condensate clouds just south of P1 that are likely pyrocumulus, and could be related to moisture emanating from the volcano. Further downwind, the plume is concentrated at progressively lower elevations, likely caused by aerosol detraining at plume top and/or air mass descent. Atmospheric stability profiles for P1 and P2–P3 indicate a local maximum between 3 and 5 km, where the plume resides, but do not show any clear trend that might be associated
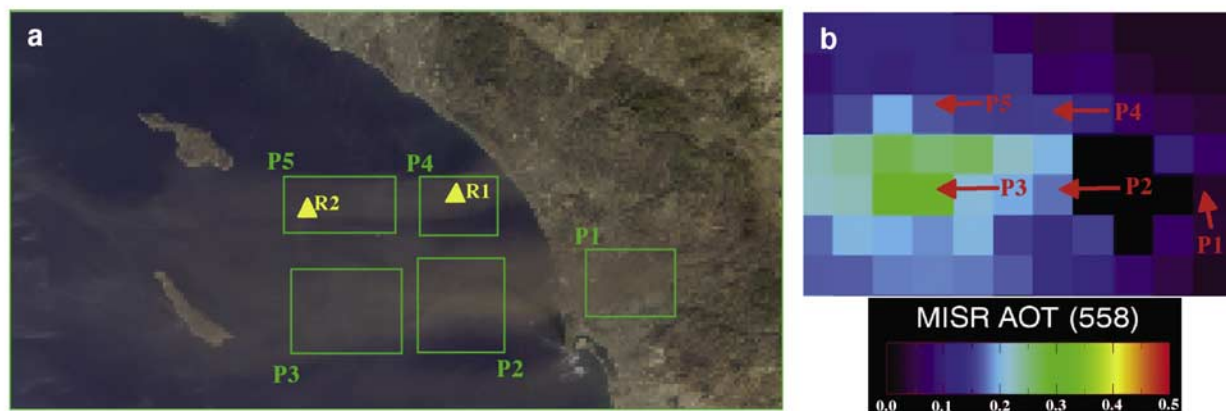
Figure 11. Southern California dust plumes, 27 November 2003, orbit 20976, path 040, block 64. (a) MISR nadir view, with five study site locations indicated as numbered green boxes. Catalina and San Clemente islands appear off the coast, and the city of Los Angeles is to the north and east, just off the top-center edge of the image. R1 and R2, marked with yellow triangles, are MISR Research Aerosol Retrieval sites. (b) MISR midvisible column AOT (version 17) retrieved at 17.6 km spatial resolution, with study site locations indicated by red arrows. For the black pixels, no retrievals were obtained.

with air mass descent producing the observed change in plume elevation. Of course, this could be a limitation of the model used. However, according to forward trajectory analysis [*Draxler and Rolph*, 2003], wind speed increases with elevation above 5.5 km, which can produce turbulent detrainment aloft as the plume evolves. A lack of detailed meteorological data stymies our ability to carry the analysis further in this case.

[42] Since volcanoes often remain active for weeks or longer, at fixed geographic locations, their plumes are especially good targets for MISR. The instrument observed Etna again 2 days later, on orbit 15233. Patch E3 on 29 October is about 50 km NE of the 27 October patch P3; the E3 height histogram and atmospheric stability curves are superposed on Figures 9c and 9f, respectively.

[43] At 3.5 km and above, on 29 October, the wind blew to the south, and the atmospheric stability peaked at about 8 km, higher than the 4.5 km peak on 27 October. According to Figure 9c, the plume ascended to 6.5 or 7.0 km, significantly higher than it did 2 days earlier, but when it reached E3, and even further downwind (not shown), it did not concentrate as high as the stability maximum identified in the NCEP profile. We see that this volcanic plume's vertical distribution reflects day-to-day changes in atmospheric stability structure, lending support to the interpretation presented in section 3.1, but other factors, most likely wind shear in this case, also affect plume vertical distribution.

3.3. Dust Over Southern California, 27 November 2003

[44] Free convection dominates the early development of the buoyant fire and volcanic aerosol plumes discussed above, but the surface shear stresses produced by regional airflows often mobilize mineral dust [e.g., *Bagnold*, 1941]. The dust plumes in Figure 11a were formed by Santa Ana winds from the ENE, which are common in southern California during October and November, when these data were taken. Major wildfires occurred here earlier in the

season (for example, Figure 6j), and the lack of ground cover contributed to the atmospheric dust loading that year.

[45] The west-pointing plumes in Figure 11 align with the near-surface wind vectors obtained from the HYSPLIT model; above about 2 km, the wind direction turns abruptly toward the south [*Draxler and Rolph*, 2003]. As with the previous examples, the plume aerosols exhibit optical properties distinct from those of the background aerosol, based on the MISR Standard aerosol retrieval: higher AOT, lower ANG, and lower SSA (Table 2 and Figure 11b). At least 40% of the midvisible optical depth is assigned to nonspherical dust particles; the remainder are mostly non-absorbing spherical particles having $r_{eff} \sim 0.12~\mu m$, typical of the background aerosol.

[46] These dust plumes are optically thinner and more diffuse than the wildfire and volcano plumes analyzed above. The MISR Standard Stereo product has limited sensitivity to diffuse hazes: an observation similar to that made for condensate cloud height retrievals by *Naud et al.* [2002]. The MISR Standard Stereo Height algorithm acquired very few significant matches using the nadir and near-nadir cameras in this case. Therefore we used the MISR Research Stereo Height Retrieval algorithm (Table 4) to derive plume elevation with the 60 and 71° forward and aft-viewing image data, which observe the scene through air-mass factors of 2 and 3, respectively. In addition to providing greater sensitivity to thin hazes due to the increased atmospheric path length, the steeper view angles generate plume height with a vertical resolution about twice as fine as that of the Standard Stereo Height product.

[47] The results for four of the patches identified in Figure 11a are given in Figures 12a–12d, and the atmospheric stability profile is shown in Figure 12e. Retrieved heights in patch 3 are similar to those for patch 2, but the plume in patch 3 had too few feature matches to produce a useful histogram. Note also that the vertical scale for all the Figure 12 height histograms is compressed and the reso-

Table 4. Comparison Between MISR Standard and Research Height Retrieval Algorithm Characteristics

MISR Stereo Height	Standard Retrieval[a]	Research Retrieval
Cameras Used for Parallax Determination	26° forward & aft, + nadir	Any two pairs, including highly oblique ones
Stereo Matcher for Heights	Area cross-correlation matcher, M23	Area cross-correlation matcher, M23
Wind Retrieval Matcher	NestedMax feature matcher, fast but can be noisy	Area cross-correlation matcher, M23

[a]Version 4.0 and higher.

lution increased relative to those in Figures 4 and 9; the double-solid line and arrow indicate the section of the stability profile covered by the histograms. Although there is a locally stable layer between about 5.5 and 7.5 km above the geoid, in the absence of sufficient buoyant lofting, the dust plume is confined to the near-surface stable layer, between about 0.5 and 2 km. The plumes in Figure 11 do not exhibit the convective texture typical airborne dust layers receiving sufficient diabatic heating to initiate free convection and lofting downwind, as can happen to thicker dust clouds on Earth, and is quite common on Mars [e.g., *Zurek et al.*, 1992].

[48] The MISR Research Aerosol Retrieval algorithm is also of considerable value in extracting aerosol microphysical properties from diffuse aerosol layers, since it allows us to analyze uniform patches as small as the pixel resolution, to select particle components and mixtures for the retrieval climatology at will, and to freely experiment with aerosol mixture acceptance criteria (Table 5; *Kahn et al.* [2001]). Research Retrieval results for 3.3×3.3 km patches R1 and R2, labeled in Figure 11a, are given in Table 2. These patches were selected for their spatial and angle-to-angle uniformity, combined with relatively high AOT, which accounts for differences between these and the larger retrieval regions analyzed by the MISR Standard Aerosol algorithm. From a very wide range of aerosol components and mixtures, the research algorithm selected 40–45% of

the medium, weakly absorbing grains obtained by the standard algorithm in the plume core. But the research algorithm also identified 55–60% coarse-mode particles, spheroidal dust analogs, and large, spherical, somewhat absorbing background particles.

[49] Illustrating plumes from globally significant dust sources, Figure 13 gives two typical examples of Saharan dust outbreaks: one at the Bodele Depression in Chad, a major dust-producing region, and one transported over the Atlantic Ocean past Western Sahara and Mauritania. For the Bodele case, the midvisible AOT is between 1.5 and about 2.5. With dust lifted by regional winds near the source, the plume is confined to the lowest 500 m of the atmosphere, based on MISR Standard products (Figures 13a–13c). The transported dust (Figures 13d–13f) has been lofted up to a layer between about 1.5 and 3 km, a region of relative stability above the boundary layer.

[50] The dust plume analyses again support the interpretation of plume vertical structure presented in section 3.1, in this case showing aerosol lifted by regional wind, that has not received additional buoyancy or dynamical mixing, remains in the boundary layer; turbulent mixing usually spreads it rapidly throughout the boundary layer. Transported dust can be lofted to layers of relative stability above the boundary layer, with turbulent mixing, diabatic heating of the airborne dust, and/or vertical advection of the air mass on regional scales, contributing to the plume's vertical
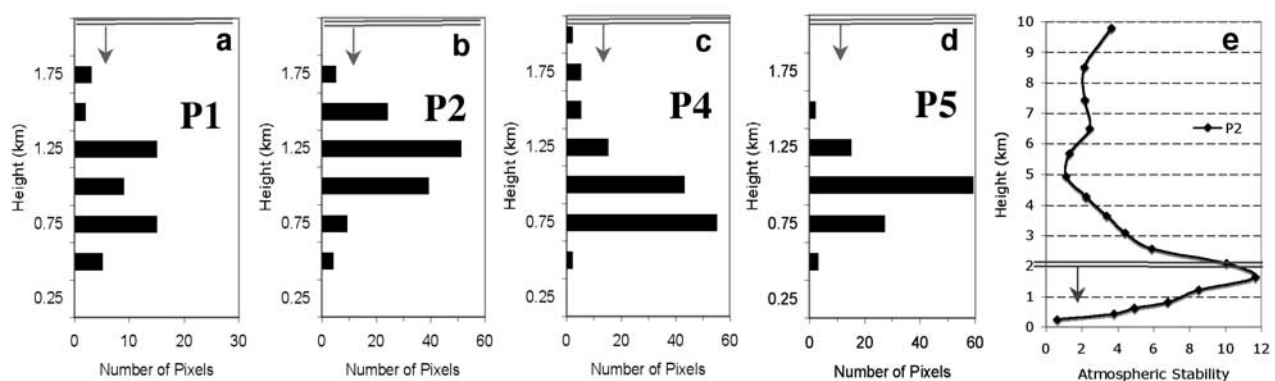

Figure 12. (a–d) Histograms of plume height, retrieved at 1.1 km horizontal resolution, and about 0.25 km vertical resolution, for four study sites identified in Figure 10a. Values for patch 3 are similar to those shown for patch 2. Note that in this case, the data were obtained with the MISR Research Plume Height Algorithm, using the most steeply viewing MISR cameras, providing greater definition to these low-AOT plumes, and yielding higher vertical resolution than the standard algorithm. Also, the vertical axis extends to only 2 km, since the plumes reside below this elevation. (e) Atmospheric stability profiles derived from the NCEP GDAS [*Saha et al.*, 2005], at about 50 km horizontal resolution, assessed in the vicinity of patch 2, to an elevation of 10 km. The double-solid lines indicate the portion of the profile captured by the histograms in this figure.

Table 5. Comparison Between MISR Standard and Research Aerosol Retrieval Algorithm Characteristics

MISR Aerosol	Standard Retrieval	Research Retrieval
Retrieval Spatial Resolution	Predetermined 16 × 16 pixel (17.6 km) regions	Arbitrary choice, down to single (usually at least 3 × 3) pixels[a]
Retrieval Spatial Coverage	Entire globe about once per week, automatically	Individual patches, user specified[a]
Aerosol Components	Predetermined by algorithm climatology; up to several tens	Arbitrary choice; up to hundreds[a]
Number Components per Mixture	Up to three	Up to four
Number of Mixtures in Comparison Space	Predetermined by algorithm climatology; up to ~100	Arbitrary choice, up to tens of thousands[a]
Surface Boundary Condition	Predetermined by algorithm logic, for either land or water	Arbitrary choice[a]
Mixture Acceptance Criteria	Predetermined by algorithm logic	Arbitrary choice[a]
Cloud Screening	Predetermined by algorithm logic	Arbitrary choice[a]
References	*Martonchik et al.* [1998, 2002]	*Kahn et al.* [2001]

[a]Must be specified individually for each patch; the choice can be constrained by any available data or other considerations.

evolution, as it does in the dusty atmosphere of Mars [e.g., *Kahn et al.*, 1992; *Zurek et al.*, 1992].

4. Discussion and Conclusions

[51] We showed that space-based multiangle and multi-spectral imaging produced by MISR can be used to determine wildfire, volcano, and dust plume physical characteristics near their sources. Regional and larger-scale aerosol transport models are usually initialized with specified aerosol amount, aerosol type, and injection height. When an aerosol source plume is captured in the instrument field-of-view, MISR provides some information about each of these quantities; we also examined the implications of the vertical structure measurements for plume dynamics.

[52] MISR aerosol retrievals used in this paper (version 17) contain sufficient particle microphysical property information to distinguish plume from background aerosols in the vicinity of the sources. Along with plume optical thickness, the particle size, SSA, and for the volcanic and dust plumes, shape, are distinct from those of the surrounding, and reflect expected source aerosol characteristics. The AOT is a measure of aerosol amount, whereas the aggregate of particle property constraints distinguishes aerosol air mass types. Globally, there is likely a sampling bias because the satellite cannot retrieve aerosol properties in cloudy pixels. However, wildfires tend to form in high-pressure, low-cloud meteorological conditions; under scattered or even broken cloud circumstances, the MISR algorithm can often retrieve aerosol amount and properties useful for this kind of analysis from nearby cloud-free pixels.

[53] As might be expected, dynamical heat flux at the source, plus the atmospheric structure, dominate plume injection height, whereas plume elevation after initial injection is controlled mainly by atmospheric structure unless the plume subsequently receives diabatic heating. Plume aerosols tend to accumulate in relatively stable atmospheric layers since the particles can more easily dissipate above, and are not easily mixed downward from these layers. For typical wildfire and volcano cases, when the plume sources are heated sufficiently relative to the surrounding air, aerosols rise toward the tops of locally stable atmospheric regions high above the boundary layer and accumulate in discrete layers. Plumes lacking sufficient buoyancy remain in the boundary layer.

[54] On the basis of this mechanism, MISR-retrieved plume height immediately downwind of the source, combined in a simple thermodynamic model with parameterized entrainment, and atmospheric stability from another source (such as the NCEP model), produces a first-order constraint on the dynamical heat flux driving plume buoyancy. This physics is typically included in plume-resolving models. However, larger-scale chemical transport models sometimes assume that aerosol plumes travel upward to altitudes determined only by an empirical correlation with the initial buoyancy, independent of the atmospheric stability structure, and/or that the aerosol is uniformly distributed even when it reaches heights above the boundary layer. The observations presented here suggest that atmospheric stability must be taken into account as well.

[55] Wind-shear-induced turbulent mixing near the layer top is one factor that can dissipate the aerosol aloft as the plume evolves. Vertical advection forced by regional meteorology [e.g., *Fromm and Servranckx*, 2003], turbulent mixing, and air entrained from the plume surroundings, are also known to play key roles in early stage aerosol plume evolution for some situations.

[56] For aerosol plumes having low AOT, diffuse features, or residing over bright, complex surfaces, such as some desert dust and most urban particle pollution, MISR Research Aerosol and Stereo Height algorithms provide needed sensitivity beyond that of the Standard MISR algorithms.

[57] MISR's once-weekly global sampling is still a limitation for studying specific, short-lived events. For example, the Quebec fires studied by *Colarco et al.* [2004], and described in section 1, fell within the MODIS field of view, but west of the MISR swath on 6 July 2002, so stereo-derived plume heights are not available for the event. However, a key conclusion of the current paper addresses the relationship between aerosol plume elevation and atmospheric stability profile. Figure 14a shows the MODIS natural color image that includes the Quebec fires on 6 July. A major smoke accumulation in the Adarondak Mountains is highlighted with a green box, and a red box identifies a region of fire fronts, for which the MODIS Thermal Anomaly product (MOD14) reported, with high confidence, fire locations (thin red annotations within the box). Another large smoke plume is centered near P2, though the MODIS fire mapper did not detect any fire anomalies in that region. Figure 14b gives NCEP reanalysis stability profiles for the
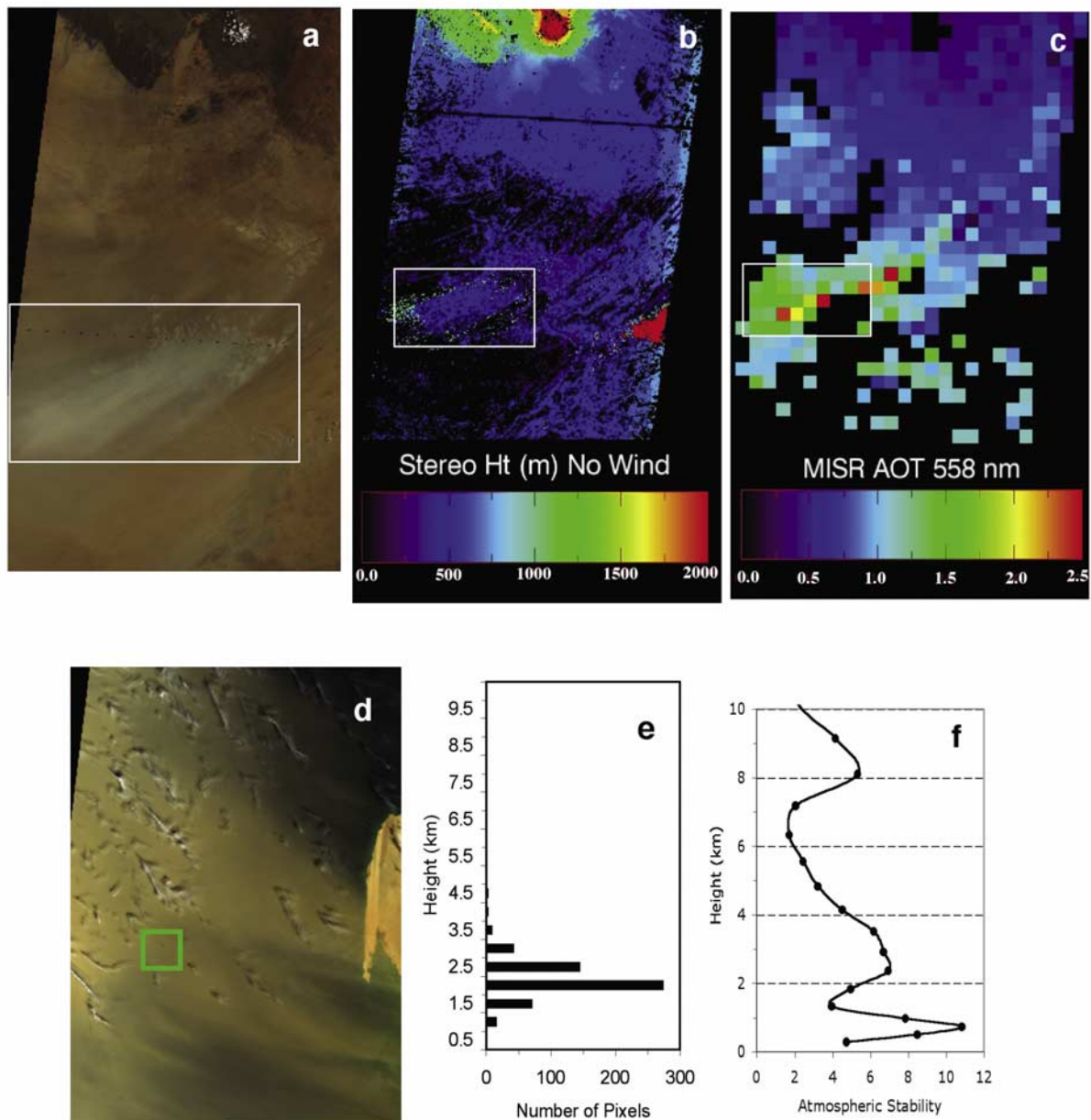
Figure 13. Source Region and Transported Saharan dust plumes. (a–c) 3 June 2005 Bodele Depression dust storm (about $15-20°$ N lat, $16-25°$ E lon), orbit 29038, path 183, blocks $75-78$. (a) MISR true-color nadir image, storm area indicated with a white box. (b) MISR Standard Stereo Height (version 13), without wind correction (labeled "no wind" in the figure), for the study area. The plume pixels are all in the lowest (500 m) bin. (c) MISR Standard 558 nm AOT for the study area. (d–f) 4 March 2004 transported Saharan dust off the coast of Western Sahara and Mauritania (about $19-24°$ N lat, -16 to $-20.5°$ W lon), orbit 22399, path 207, blocks $72-75$. (d) MISR true-color nadir image with study patch marked in green. (e) Plume height histogram for the study patch, from MISR Standard Stereo Height product. (f) Atmospheric stability profile, calculated from the NCEP GDAS [*Saha et al.*, 2005] using equations (1a) and (1b).

same date, at times bracketing the Terra overpass, covering the P2 smoke region at coarse spatial resolution (2.5°); plots for nearby NCEP grid cells have similar vertical structure. On the basis of the observations presented in this paper for cases having MISR Stereo Height measurements, arrows are placed at likely elevations for smoke plume concentrations. MODIS did not identify large thermal anomalies under the

thickest smoke on 6 July, and peak radiant energy flux of about 200 W/m^2 was reported within the red box in Figure 14a, where anomalies were detected. The simple analysis given in section 3.1.5 suggests that, in light of Figure 14b, the most intense sources of the Quebec smoke plume on 6 July may have had enough dynamical heat flux to reach locally stable layers around 3 km, but not likely
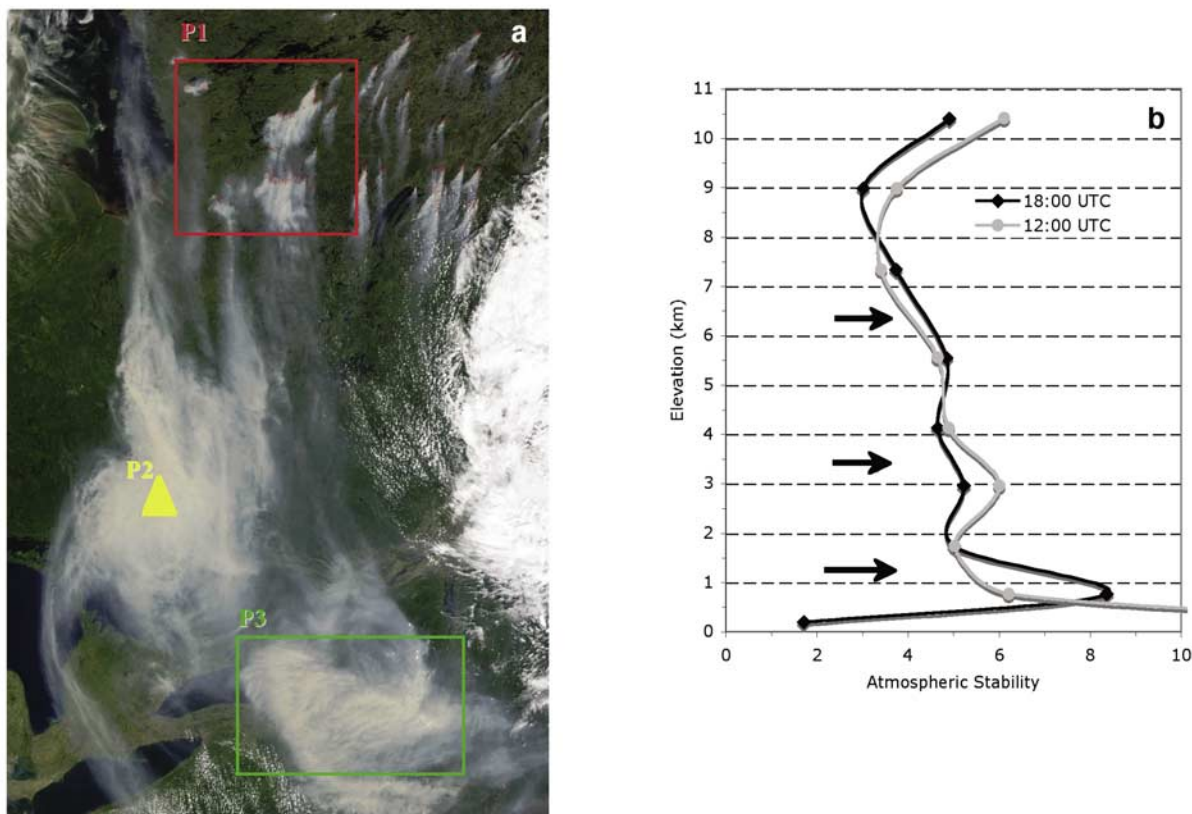
Figure 14. Quebec and Adarondak fires, 6 July 2002. (a) MODIS natural color image showing the Quebec fire region (red box) and more isolated wildfire fronts to the E, that were detected by the MODIS fire mapper (thin red annotations within and outside the red box). A large Quebec smoke plume is centered on P2, but the MODIS fire mapper did not detect any sources in that region. The Adarondak smoke plume appears SSE of the Quebec fires (green box), and was imaged by MISR too. The Quebec fire region was west of the MISR swath on this day (Image from the MODIS Rapid Response site http://rapidfire.sci.gsfc.nasa.gov/). (b) Atmospheric stability profiles derived from NCEP reanalysis model results (2.5° horizontal resolution), centered at 47.5°N, 80.0°W (near the yellow triangle, P2), at 12:00 UTC (gray) and 18:00 UTC (black), bracketing the Terra satellite overpass at 15:50 UTC. Arrows indicate likely vertical positions for smoke plume concentrations, based on cases presented for which MISR Stereo Heights are available; as discussed in the text, the actual plume elevation also depends upon the dynamical heat flux at the source, and other factors.

higher, giving independent, though partly model-driven, support to the conjecture of *Colarco et al.* [2004] that injection was weaker on 6 July than on earlier days.

[58] Despite serendipitous coverage of specific events, MISR's current data record, more than 6 years long, covers most of the planet over 300 times, enough to assess patterns of aerosol source plume initial characteristics, subsequent development, regional effects, and larger-scale impacts. Several groups are now using MISR aerosol plume heights, along with other data, for a range of applications. For example, using MISR, MODIS, and TOMS retrievals, (Fromm et al., Stratospheric Impact of the Chisholm PyroCb: A satellite and lidar perspective, in preparation, 2007) examine the height, horizontal spatial distribution, and implied aerosol-severe storm interactions for the May 2001, very high-elevation Chisholm Fire smoke plume in Alberta, Canada. *Stenchikov et al.* [2006] use the New York World Trade Center fire plume's three-dimensional aerosol distribution on 12 September 2001, obtained from

MISR, to constrain a detailed model simulation of the aerosol response to regional meteorology.

[59] The calculations in section 3, relating MISR-observed plume height and atmospheric stability structure to dynamical heat flux at the source, point toward an effort, beyond the scope of the current paper, aimed at capturing finer differences among fire events, such as determining quantitative relationships between dynamical heat flux related to MISR plume height and radiant energy flux observed by MODIS, for different fire types, and exploring the split in aerosol amount between boundary layer smoke and higher-elevation plumes, constrained by the stereo heights (for example, Figures 4e and 9e). These require finer-scale meteorological constraints, and an advanced model or models to more accurately estimate entrainment based on environmental factors, take account of fuel and fire characteristics, fire front heterogeneity, and possibly include moist convection, plume radial structure, synoptic-scale winds, and dynamical feedbacks. A fully three-dimensional calculation might be

warranted to simulate the observational constraints on complex fire fronts that involve horizontal distributions of flaming and smoldering phases (for example, Figure 6d).

[60] On the basis of the results of this paper, a MISR climatology of aerosol plume behavior is being developed.

References

Abdou, W. A., D. J. Diner, J. V. Martonchik, C. J. Bruegge, R. A. Kahn, B. J. Gaitley, K. A. Crean, L. A. Remer, and B. Holben (2005), Comparison of coincident MISR and MODIS aerosol optical depths over land and ocean scenes containing AERONET sites, *J. Geophys. Res.*, 110, D10S07, doi:10.1029/2004JD004693.

Ackerman, T. P., A. J. Braverman, D. J. Diner, T. L. Anderson, R. A. Kahn, J. V. Martonchik, J. E. Penner, P. J. Rasch, B. A. Wielicki, and B. Yu (2004), Integrating and interpreting aerosol observations and models within the PARAGON framework, *Bull. Am. Meteorol. Soc.*, 85, 1523–1533.

Akimoto, H. (2003), Global air quality and pollution, *Science*, 302, 1716–1719.

Bagnold, R. A. (1941), *The Physics of Blown Sand and Desert Dunes*, Methuen Press, London.

Clark, T. L., M. A. Jenkins, J. Coen, and D. Packham (1996), A coupled atmosphere-fire model: Convective feedback on the fire-line dynamics, *J. Appl. Meteorol.*, 35, 875–901.

Colarco, P. R., M. R. Schoeberl, B. G. Doddridge, L. T. Marufu, O. Torres, and E. J. Welton (2004), Transport of smoke from Canadian forest fires to the surface near Washington, D.C.: Injection height, entrainment, and optical properties, *J. Geophys. Res.*, 109, D06203, doi:10.1029/2003JD004248.

Cotton, W. R., et al. (2003), RAMS 2001: Current status and future directions, *Meteorol. Atmos. Phys.*, 82, 5–29.

Diner, D. J., R. Davies, L. DiGirolamo, A. Horvath, C. Moroney, J.-P. Muller, S. R. Paradise, D. Wenkert, and J. Zong (1999), MISR level 2 cloud detection and classification algorithm theoretical basis, JPL D-11399, Rev. D, Jet Propulsion Laboratory, California Institute of Technology.

Diner, D. J., et al. (2005), The value of multi-angle measurements for retrieving structurally and radiatively consistent properties of clouds, aerosols, and surfaces, *Remote Sens. Environ.*, 97, 495–518.

Draxler, R. R., and G. D. Rolph (2003), Hybrid Single-Particle Lagrangian Integrated Trajectory (HYSPLIT) Model access via the NOAA Website http://www.arl.noaa.gov/ready/hysplit4.html, NOAA Air Resources Laboratory, Silver Spring, MD.

Fromm, M. D., and R. Servranckx (2003), Transport of fire smoke above the tropopause by supercell convection, *Geophys. Res. Lett.*, 30(10), 1542, doi:10.1029/2002GL016820.

Giglio, L. (2005), MODIS Collection 4 Active Fire Product User's Guide, Version 2.0, May 2005. (http://modis-fire.umd.edu/)

Ginoux, P., M. Chin, I. Tegen, J. Prospero, B. Holben, and S.-J. Lin (2001), Sources and distributions of dust aerosols simulated with the GOCART model, *J. Geophys. Res.*, 106, 20,255–20,273.

Glaze, L. S., S. M. Bologa, and L. Wilson (1997), Transport of atmospheric water vapor by volcanic eruption columns, *J. Geophys. Res.*, 102, 6099–6108.

Holton, J. R. (1992), *An Introduction to Dynamic Meteorology*, pp. 511, Elsevier New York.

Intergovernmental Panel on Climate Change (IPCC) (2001), *Climate Change 2001: The Scientific Basis*, edited by J. T. Houghton, et al., 881 pp., Cambridge Univ. Press.

Justice, C. O., L. Giglio, S. Koronitzi, J. Owens, J. Morisette, D. Roy, J. Descloitres, S. Alleaume, F. Petitcolin, and Y. Kaufman (2002), The MODIS fire products, *Remote Sens. Environ.*, 83, 244–262.

Kahn, R., S. W. Lee, T. Z. Martin, and R. W. Zurek (1992), The Martian Dust Cycle, in *Mars*, edited by H. H. Kieffer, B. M. Jakosky, C. W. Snyder, and M. S. Matthews, pp. 1017–1053, Univ. of Ariz. Press, Tucson.

Kahn, R., P. Banerjee, and D. McDonald (2001), The sensitivity of multi-angle imaging to natural mixtures of aerosols over ocean, *J. Geophys. Res.*, 106, 18,219–18,238.

Kahn, R., B. Gaitley, J. Martonchik, D. Diner, K. Crean, and B. Holben (2005), MISR global aerosol optical depth validation based on two years of coincident AERONET observations, *J. Geophys. Res.*, 110, D10S04, doi:10.1029/2004JD004706.

Kalashnikova, O. V., and R. A. Kahn (2006), The ability of multi-angle remote sensing observations to identify and distinguish mineral dust types: Part 2. Sensitivity data analysis, *J. Geophys. Res.*, 111, D11207, doi:10.1029/2005JD006756.

Kaufman, Y. J., C. O. Justice, L. P. Flynn, J. D. Kendall, E. M. Prins, L. Giolio, D. E. Ward, W. P. Menxel, and A. W. Setzer (1998), Potential global fire monitoring from EOS-MODIS, *J. Geophys. Res.*, 103, 32,215–32,238.

Kaufman, Y. J., C. Ichoku, L. Giglio, S. Korontzi, D. A. Chu, W. M. Hao, R.-R. Li, and C. O. Justice (2003), Fire and smoke observed from the Earth Observing System MODIS instrument—Products, validation, and operational use, *Int. J. Remote Sens.*, 24, 1765–1781.

Lavoué, D., C. Liousse, H. Cachier, B. J. Stocks, and J. G. Goldammer (2000), Modeling of carbonaceous particles emitted by boreal and temperate wildfires at northern latitudes, *J. Geophys. Res.*, 105(D22), 26,871–26,890, doi:10.1029/2000JD900180.

Martonchik, J. V., D. J. Diner, R. Kahn, M. M. Verstraete, B. Pinty, H. R. Gordon, and T. P. Ackerman (1998), Techniques for the retrieval of aerosol properties over land ocean using multiangle data, *IEEE Trans. Geosci. Remote Sens.*, 36, 1212–1227.

Martonchik, J. V., D. J. Diner, K. Crean, and M. Bull (2002), Regional aerosol retrieval results from MISR, *IEEE Trans. Geosci. Remote Sens.*, 40, 1520–1531.

Martonchik, J. V., D. J. Diner, R. A. Kahn, B. J. Gaitley, and B. N. Holben (2004), Comparison of MISR and AERONET aerosol optical depths over desert sites, *Geophys. Res. Lett.*, 31, L16102 doi:10.1029/2004GL019807.

Mazzoni, D., J. Logan, D. Diner, R. Kahn, L. Tong, and Q. Li (2007), A data-mining approach to cataloging smoke plumes from MISR and MODIS data, *Remote Sens. Environ.*, 107, 138–158.

Moroney, C., R. Davies, and J.-P. Muller (2002), MISR stereoscopic image matchers: Techniques and results, *IEEE Trans. Geosci. Remote Sens.*, 40, 1547–1559.

Morton, B. R., G. I. Taylor, and J. S. Turner (1956), Turbulent gravitational convection from maintained and instantaneous sources, *Proc. R. Soc. London, Ser. A*, 234, 1–23.

Muller, J.-P., A. Mandanayake, C. Moroney, R. Davies, D. J. Diner, and S. Paradise (2002), Operational retrieval of cloud-top heights using MISR data, *IEEE Trans. Geosci. Remote Sens.*, 40, 1532–1546.

Naud, C., J.-P. Muller, and E. E. Clothiaux (2002), Comparison of cloud top heights derived from MISR stereo and MODIS CO2-slicing, *Geophys. Res. Lett.*, 29(16), 1795, doi:10.1029/2002GL015460.

Naud, C., J. Muller, M. Haeffelin, Y. Morille, and A. Delaval (2004), Assessment of MISR and MODIS cloud top heights through inter-comparison with a back-scattering lidar at SIRTA, *Geophys. Res. Lett.*, 31, L04114, doi:10.1029/2003GL018976.

Naud, C., J.-P. Muller, E. E. Clothiaux, B. A. Baum, and W. P. Menzel (2005), Intercomparison of multiple years of MODIS, MISR, and radar cloud-top heights, *Ann. Geophys.*, 23, 2415–2424.

Penner, J. E., R. J. Charlson, J. M. Hales, N. S. Laulainen, R. Liefer, T. Novakov, J. Ogren, L. F. Radke, S. E. Schwartz, and L. Travis (1994), Quantifying and minimizing uncertainty if climate forcing by anthropogenic aerosols, *Bull. Am. Meteorol. Soc.*, 75, 375–400.

Rasch, P. J., W. D. Collins, and B. E. Eaton (2001), Understanding the Indian Ocean Experiment (INDOEX) aerosol distributions with an aerosol assimilation, *J. Geophys. Res.*, 106, 7337–7355.

Saha, S., et al. (2005), The NCEP climate forecast system, *J. Clim.*, in press.

Seiz, G., and R. Davies (2006), Reconstruction of cloud geometry from multi-view satellite images, *Remote Sens. Environ.*, 100(2), 143–149.

Seiz, G., R. Davies, and A. Grun (2007), Stereo cloud-top height retrieval with ASTER and MISR, *Int. J. Remote Sens.*, 27(9–10), 1839–1853.

Small, R. D., and K. E. Heikes (1988), Early cloud formation by large area fires, *J. Appl. Meteorol.*, 27, 654–663.

Stenchikov, G., N. Lahoti, P. J. Lioy, P. G. Georgopoulos, D. J. Diner, and R. Kahn (2006), Multiscale plume transport from collapse of the World Trade Center on September 11, 2001, *Environ. Fluid Mech.*, 6(5), 425–450.

Trentamnn, J., G. Luderer, T. Winterrath, M. D. Fromm, R. Servanckx, C. Textor, M. Herzog, H.-F. Graf, and M. O. Andreae (2006), Modeling of biomass smoke injection into the lower stratosphere by a large forest fire: Part 1. Reference simulation, *Atmos. Chem. Phys. Discuss.*, *6*, 6041–6080.

Weihs, D., and R. D. Small (1993), An approximate model of atmospheric plumes produced by large area fires, *Atmos. Environ.*, *27A*, 73–82.

Westphal, D. L., and O. B. Toon (1991), Simulations of microphysical, radiative, and dynamical processes in a continental-scale forest fire smoke plume, *J. Geophys. Res.*, *96*, 22,379–22,400.

Zurek, R. W., J. R. Barnes, R. M. Haberle, J. E. Tillman, and C. B. Leovy (1992), Dynamics of the atmosphere of Mars, in *Mars*, edited by H. H. Kieffer, B. M. Jakosky, C. W. Snyder, and M. S. Matthews, pp. 835–933, Univ. of Ariz. Press, Tucson.

————————————

D. J. Diner, E. Fishbein, R. A. Kahn, W.-H. Li, J. V. Martonchik, and C. Moroney, Jet Propulsion Laboratory, California Institute of Technology, 4800, Oak Grove Drive, Pasadena, CA 91109, USA. (ralph.kahn@jpl.nasa.gov)